The Thermal Memory of Reionization

Sudhir Raskutti

Supervised by
Professor Stuart Wyithe

School of Physics
Faculty of Science
University of Melbourne

30 August, 2011

Submitted in total fulfilment of the requirements of the degree of
Master of Philosophy

Abstract

The reionisation of cosmic hydrogen represents a significant moment in the history of the Universe. The appearance of the first stars and quasars heated and ionised the intergalactic medium (IGM), catalysing the transition in which intergalactic hydrogen changed from being predominantly neutral to its present day, highly ionised state. Understanding exactly how and when this phase transition occurred will offer significant insight into the nature of the first sources of light. Measurements of temperature in the IGM provide a potentially powerful constraint on reionisation history due to the thermal imprint left by photo-ionisation of neutral hydrogen. However, until only recently, IGM temperature measurements were limited to redshifts $2 \leq z \leq 4.5$, restricting the ability of these data to probe the reionisation history at $z > 6$. In this work, we use the first direct measurements of IGM temperature in quasar proximity zones at $z \sim 5.5 - 6.5$ to establish new constraints on the redshift at which inhomogeneous hydrogen reionisation completed.

We utilise a semi-numerical reionisation model to trace the propagation into the IGM of H I ionisation fronts produced by stellar sources. Then, calibrating the model to reproduce observational constraints on the electron scattering optical depth and the H I photoionisation rate, we compute the resulting spatially inhomogeneous temperature distribution at $z = 6$ for a variety of reionisation scenarios. Under suitable assumptions for the ionising spectra of population II sources, we determine that for reionization scenarios complete by $z_{\rm r} > 9.0$, the IGM settles to roughly the same asymptotic thermal state at $z = 6.0$ irrespective of when reionization occured. However, for $z_{\rm r} < 9.0$, the ionization of neutral hydrogen leaves behind an imprint, that is still up to $5\,000\mathrm{K}$ above the thermal asymptote at $z = 6.0$. Using our models, and the temperature measurements around quasar proximity zones, we constrain the redshift by which reionisation was completed to be $z_{\rm r} > 7.9(6.5)$ at $68(95)$ per cent confidence. We conclude that future temperature measurements around other high redshift quasars will increase the power of this technique, enabling us to both tighten and generalise this result.

This is to certify that:

- the thesis comprises only my original work towards the MPhil
- due acknowledgement has been made in the text to all other material used,
- the thesis is less than 50,000 words in length, exclusive of tables, maps, bibliographies and appendices

Sudhir Raskutti

Acknowledgments

First and foremost, I would like to thank my supervisor Stuart Wyithe for all his help and advice over the past year and a half. Not only for this thesis, but for all matters academic, his support has been invaluable. Just as importantly, I am very grateful to Jamie Bolton for providing his constant advice and technical expertise, and for proof reading earlier versions of this thesis. In addition, many thanks to my other collaborators Martin Haehnelt, George Becker and Paul Geil, whose code was the foundation of much of my work.

I am deeply indebted also to my friends and family for making the past 18 months so enjoyable. In particular to everyone in Room 359, and down the corridor as well, thank you for ensuring that coming to work was never a chore and that my time and money was always spent in the most productive way. Finally, a special thank you to all my family, to Mum and Dad for their help and interest, to Garvesh for his help on all things statistical and Kiran for ensuring that my knowledge of basic physics was not forgotten.

Contents

1 Introduction **9**
- 1.1 A Mathematical Description of the Universe . . . 10
- 1.2 The Growth of Structure . . . 11
  - 1.2.1 Linear Gravitational Growth . . . 12
  - 1.2.2 Formation of Nonlinear Objects . . . 13
- 1.3 The Epoch of Reionization (EoR) . . . 14
  - 1.3.1 The Sources Behind Reionization . . . 15
  - 1.3.2 The topology of Reionization . . . 15
- 1.4 Observational Probes of the EoR . . . 17
  - 1.4.1 Gunn-Peterson Trough . . . 17
  - 1.4.2 Thomson Optical Depth . . . 20
- 1.5 Temperature as a Probe of the EoR . . . 20
  - 1.5.1 Previous work . . . 21
- 1.6 Thesis Outline . . . 23

2 Semi-Numerical Reionisation Model **24**
- 2.1 Construction of Density Field . . . 24
- 2.2 Ionisation model . . . 25
- 2.3 The ionising emissivity . . . 27
- 2.4 The ionising background specific intensity . . . 28
  - 2.4.1 The pre-overlap mean free path . . . 28
  - 2.4.2 The post-overlap mean free path . . . 30
- 2.5 Thermal evolution . . . 31
- 2.6 Inclusion of quasar heating . . . 33

3 Modelling of ionising sources **35**
- 3.1 Observational constraints on $N_{\rm ion}$ . . . 35
  - 3.1.1 The ionisation rate from the Lyα forest opacity . . . 35

3.1.2 Thomson Optical Depth to CMB Photons 37
3.2 Parametrisation of $N_{\rm ion}$ 37
3.2.1 Linear Model 38
3.2.2 Cubic Model 40

4 Results **42**
4.1 The IGM thermal state following reionisation 42
4.2 The Redshift of Reionization 42
4.2.1 The Temperature-Density Relation 44
4.2.2 Different Reionization Scenarios 45
4.3 Temperature in a Quasar Proximity Zone 47
4.3.1 Comparisons 48
4.3.2 Quasar Density Bias 51

5 Constraints on Reionisation History **53**
5.1 Constraints from the measured temperatures 54
5.2 Constraints from upcoming temperature measurements 59

6 Conclusions **62**

List of Figures

1.1 The Gunn-Peterson Trough in high redshift quasars. Figure taken from Becker et al. (2001) . . . 18
1.2 Thermal evolution of the IGM for different reionization scenarios. Figure taken from Hui & Haiman (2003) . . . 21
1.3 The IGM thermal asymptote. Figure taken from Hui & Haiman (2003) . 22

2.1 Redshift evolution of the Clumping Factor in hydrodynamical simulations. Figure taken from Pawlik et al. (2009) . . . 26
2.2 Calculated H I bubble sizes at different stages of reionization . . . 29

3.1 Constraints on the redshift evolution of H I and $N_{\rm ion}$ from existing observations. Figure taken from Mitra et al. (2011) . . . 39
3.2 Optimal evolution of of H I and $N_{\rm ion}$ from our semi-numerical model . . 41

4.1 Modelled evolution of the ionization fraction and temperature in an inhomogenous IGM . . . 43
4.2 Evolution of the ionization fraction and temperature in an inhomogenous IGM taken from hydrodynamical simulations. Figure taken from Trac et al. (2008) . . . 43
4.3 Modelled behaviour of the temperature-density relation at $z = 6$ for early and late reionization scenarios . . . 44
4.4 Behaviour of the temperature-density relation at $z = 6$ for early and late reionization scenarios in hydrodynamical simulations. Figure taken from Trac et al. (2008) . . . 45
4.5 Modelled evolution of the ionization fraction, temperature and temperature-density relation for early and late reionization scenarios and different ionizing models . . . 46
4.6 Statistics of the IGM temperature distribution as a function of reionization time for the whole IGM . . . 48

4.7 Observations of temperature around high redshift quasars. Figure taken from Bolton et al. (2011) 49
4.8 Statistics of the modelled temperature distribution around high redshift quasars as a function of reionization redshift 50

5.1 Model dependent constraints on the reionization redshift based on high redshift observation of temperatures around quasars 55
5.2 Model averaged constraints on the reionization redshift based on high redshift observation of temperatures around quasars 57
5.3 Model averaged estimates of the most probable reionization redshifts and quasar spectral indices 58
5.4 Bias and uncertainty in future predictions of the reionization redshift inferred from quasar temperatures 59

List of Tables

3.1 Photo-ionisation rate constraints from the Lyα forest opacity obtained by Bolton et al. (2005) and Wyithe & Bolton (2010) 36

5.1 Bayesian model probabilities as well as 1 and 2-σ constraints on the reionization redshift for different reionization models 56

Chapter 1

Introduction

Our understanding of the universe, and the matter from which it is comprised, has progressed significantly over the past decade. Observations of the the relationship between redshift and luminosity distance in Type Ia supernovae (Perlmutter et al., 1999; Riess et al., 2004; Astier et al., 2006) point to an expanding universe, driven by Einstein's cosmological constant, Λ, or dark energy. Concurrent observations of weak lensing (Bacon et al., 2003; Heymans et al., 2005; Semboloni et al., 2006) and galactic rotation curves (Rubin et al., 1980) hint at the dominating presence of cold dark matter (CDM), with only a small fraction of the universe being composed of luminous baryonic matter. Together, these observations provide strong evidencefor a Big Bang ΛCDM concordance model of cosmology.

Meanwhile, data obtained from the Cosmic Microwave Background (CMB), previously from the Wilkinson Microwave Anisotropy Probe (WMAP, Spergel et al. 2003, 2007; Dunkley et al. 2009; Komatsu et al. 2011) and in the near future from Planck, offer an amazing snapshot of density fluctuations in the early universe. These perturbations, which were amplified from tiny quantum fluctuations in the early Universe to cosmological scales during a rapid expansion phase known as inflation (Guth, 1981; Linde, 1984), are thought to be the seeds of all present day structure. This picture is confirmed by numerical simulations (Peebles & Yu, 1970; Davis et al., 1985; Springel, 2005) of gravitational instability and collapse, which produce statistically plausible matter distributions from the CMB fluctuations.

In contrast, the details of early galaxy formation, from 400 million to 1 billion years after the Big Bang, are not well understood. Our best window on this epoch comes from the signature of hydrogen reionization left behind by the first sources. The appearance of the first stars and quasars irradiated the universe thereby ionizing the predominantly neutral hydrogen in the IGM. Therefore, studying the signal of this reionization event offers a means of probing the nature and formation time of the first sources of light. However, uncovering the physics of this epoch requires first and foremost an under-

standing of the structure formation preceding it and the cosmological context in which it occurs. In the following chapter, this cosmological evolution is discussed in order to provide a framework for the epoch of reionization and a scientific motivation for the work undertaken in this thesis. Throughout the thesis we use ΛCDM cosmological parameters $\Omega_{\rm m} = 0.27$, $\Omega_\Lambda = 0.73$, $\Omega_{\rm b}h^2 = 0.0225$, $h = 0.704$, $\sigma_8 = 0.81$, $n_{\rm s} = 0.96$, consistent with recent studies of the cosmic microwave background (Komatsu et al. 2011).

1.1 A Mathematical Description of the Universe

Our understanding of the universe is based on the two fundamental tenets that at the largest scales, matter and energy are both spatially homogeneous and isotropic. As the only large-scale motion compatible with these assumptions is a universal expansion or contraction, this so-called "cosmological principle" leads directly to the Hubble Law

$$\dot{\mathbf{r}} = H(t)\mathbf{r} \tag{1.1}$$

which relates the position $\mathbf{r}$ relative to an observer to its recessional velocity $\dot{\mathbf{r}}$. In this context, it makes sense to define a set of co-ordinates $\mathbf{x}$ that are comoving or static with the Hubble flow

$$\mathbf{r} \equiv a(t)\mathbf{x} \tag{1.2}$$

where $a(t)$ is referred to as the scale factor and is used to trace the Hubble expansion rate

$$H(t) \equiv \frac{\dot{a}}{a} \tag{1.3}$$

In this framework, observers at rest remain at fixed $\mathbf{x}$, with their physical separation increasing with time in proportion to $a(t)$. The Hubble expansion also has the effect of changing the frequency of observed light, so that light emitted by a source at time t is observed now with a redshift $1 + z = \frac{a_0}{a(t)}$, where we set the present day scale factor to $a_0 \equiv 1$.

When applied to Einstein's Field Equations of General Relativity, the assumptions of homogeneity and isotropy also yield the Friedman Equation (Weinberg, 1972; Turner & Kolb, 1990)

$$H^2(t) = \frac{8\pi G}{3}\rho - \frac{k}{a^2} \tag{1.4}$$

which describes the Hubble expansion in terms of the energy density ρ and the intrinsic curvature k of the universe. Dividing through by the critical density, $\rho_c = \frac{8\pi H_0^2 G}{3}$ so that

$\Omega = \frac{\rho}{\rho_c}$, and decomposing into separate matter (Ω_m), radiation (Ω_r) and dark energy (Ω_Λ) components, we obtain the more well-known form of the equation for a universe with zero curvature

$$H^2(t) = H_0^2[\Omega_m a(t)^{-3} + \Omega_r a(t)^{-4} + \Omega_\Lambda] \tag{1.5}$$

where the exponents on $a(t)$ arise from the behaviour of the different energy components under expansion. This relation, alongside measurements of the relative present-day energy densities, provide a framework with which to evaluate the growth of structure in the universe.

1.2 The Growth of Structure

In the hot Big Bang model, the Friedman equation predicts an initially hot universe dominated by radiation, where photons and ionized gas exist in a uniform plasma. At $z \approx 10^4$, we transition into the era of matter-domination, however the universe remains hot enough for photons and baryons to remain coupled by Thomson scattering. It is not until $z \approx 1100$ that the universe cools enough to allow protons and electrons to recombine into neutral hydrogen. This effectively decouples the photons from the now neutral baryons and they free stream towards us. We see the imprint of this Recombination era in these photons, which we observe today as the CMB.

The CMB informs us of an early universe that was highly uniform with small perturbations in density on the order of 10^{-5} of the mean density. This uniformity allows us to model these perturbations as a linear field of overdensities

$$\delta(\mathbf{x}, z) = \frac{\rho(\mathbf{x}, z) - \bar{\rho}(z)}{\bar{\rho}(z)} \tag{1.6}$$

for a universe of mean density $\bar{\rho}(z)$. The overdensity field also has a Fourier transform pair of fluctuations on a given scale λ defined by

$$\delta(\mathbf{x}, z) = \int \frac{d^3\mathbf{k}}{(2\pi)^3} \hat{\delta}(\mathbf{k}, t) e^{i\mathbf{k}\cdot\mathbf{x}} \tag{1.7}$$

where $k = |\mathbf{k}| = \frac{2\pi}{\lambda}$. Since fluctuations in the CMB are observed, at high precision, to be drawn from a zero-mean Gaussian distribution, the entire density field can be characterised by its primordial power spectrum $P(k, z)$ alone

$$\langle \hat{\delta}(\mathbf{k}, z), \hat{\delta}^*(\mathbf{p}, z) \rangle = P(k, z)\delta^{(3)}(\mathbf{k} - \mathbf{p}) \tag{1.8}$$

In the primordial universe, $z \to \infty$, this is measured to be $P(k, \infty) \propto k^{n_\mathrm{s}-4}$, where $n_\mathrm{s} = 0.96$.

1.2.1 LINEAR GRAVITATIONAL GROWTH

The evolution of this initial overdensity field into the complex structures we see today is highly non-trivial. However, for a significant fraction of its evolution, fluctuations in the density field remain small and so may be treated accurately with linear perturbation theory. This posits that the growth of structure is scale-free so that the density field at later times can be related to the primordial density field by separate functions, one dependent on scale alone $T(k)$ and a scale-independent growth function $D(z)$.

The transfer function $T(k)$ has a complex dependence on physics in the radiation-dominated era and the time at which a given perturbation entered the horizon. However, a number of analytic fits, which account for these, have been found (Bond & Efstathiou, 1984; Holtzman, 1989; Eisenstein & Hu, 1999) and for the remainder of this work, we will adopt the transfer function of Eisenstein & Hu (1999).

On the other hand, the growth factor may be evaluated quite easily by assuming that, in the linear regime, the energy distribution is well characterised by an ideal, pressureless fluid of particles undergoing cosmological expansion. When this is done, the evolution of the over-density field with redshift is governed by the continuity and Euler equations

$$\frac{\partial \delta}{\partial t} + \frac{1}{a}\nabla \cdot [(1+\delta)\mathbf{u}] = 0 \tag{1.9}$$

$$\frac{\partial \mathbf{u}}{\partial t} + H\mathbf{u} + \frac{1}{a}(\mathbf{u}\cdot\nabla)\mathbf{u} = -\frac{1}{a}\nabla\phi \tag{1.10}$$

where the gravitational potential ϕ is given by the Poisson equation in terms of the density perturbation

$$\nabla^2\phi = 4\pi G\bar{\rho}a^2\delta \tag{1.11}$$

For small perturbations $\delta \ll 1$, the fluid equations can be linearized and combined to yield

$$\frac{\partial^2\delta}{\partial t^2} + 2H\frac{\partial\delta}{\partial t} = 4\pi G\bar{\rho}\delta \tag{1.12}$$

This linear equation has, in general, two independent solutions, only one of which grows with time. It is this growing mode solution, which gives the growth factor (Peebles, 1980)

$$D(z) \propto \frac{\left(\Omega_\Lambda a^3 + \Omega_k a + \Omega_m\right)^{1/2}}{a^{3/2}} \int^a \frac{a^{3/2}\,da}{\left(\Omega_\Lambda a^3 + \Omega_k a + \Omega_m\right)^{3/2}}\,, \tag{1.13}$$

where we neglect Ω_r as it is negligible at redshifts of interest $z \ll 10^4$. Using this growth factor, the linear density field at later times is defined by the redshift-dependent power spectrum

$$P(k, z) \propto k^{n_s - 4} T^2(k) D^2(z) \tag{1.14}$$

1.2.2 FORMATION OF NONLINEAR OBJECTS

Eventually, the small-scale density fluctuations seen in the CMB grow to order unity, at which point the linear approximation breaks down. When this occurs, the full non-linear evolution from an initial perturbation to a collapsed dark matter halo can only be found for highly symmetric situations. In particular, for a spherically symmetric over-density, which collapses at the present day, the evolution is governed by Newtonian collapse in the presence of cosmological expansion

$$\frac{d^2 R}{dt^2} = H_0^2 \Omega_\Lambda \, R - \frac{GM}{R^2} \tag{1.15}$$

where R is the radius in proper coordinates, H_0 is the present day Hubble constant, M is the total mass enclosed within radius R, and the initial velocity field is given by the Hubble flow $dR/dt = H(t)R$. If the mass shell at radius R is bound then it reaches a radius of maximum expansion and subsequently collapses. At the moment when the over-density collapses to a point, it may be expanded to first order in time, which gives an estimate of the overdensity predicted by linear theory (Peebles, 1980). In a ΛCDM universe, this gives $\delta_L \approx 1.686$. Therefore, a spherical overdensity collapses at redshift z if its linear overdensity extrapolated to the present day, or the critical density of collapse, is

$$\delta_{\rm crit}(z) = \frac{1.686}{D(z)} \, , \tag{1.16}$$

In reality of course, no perturbation will collapse to a point but instead slight asymmetries in the initial conditions will cause the halo to virialise by violent relaxation. However, this occurs on a similar timescale to the collapse of an ideally symmetric overdensity to a point. This means that at any given redshift, we can use the linear density field alone to obtain an estimate of whether or not an overdensity at some scale R will play host to a virialised dark matter halo capable of giving rise to galaxy formation.

To do this, we recognise that we may evaluate the overdensity field at a scale R by simply filtering the original field with a spherical top-hat window of the same scale. This effectively smooths over all density scales below R and leaves behind only the information for larger haloes. The resultant field must, by construction, also be zero-mean Gaussian with a variance given by:

$$\sigma^2(R) = \int_0^\infty \frac{dk}{2\pi^2}\, k^2 P(k) \left[\frac{3j_1(kR)}{kR}\right]^2 \tag{1.17}$$

where $j_1(x) = (\sin x - x\cos x)/x^2$ is the Fourier Transform of the top-hat window function. According to the model of Press and Schechter (Press & Schechter, 1974), the fraction of virialised haloes with radius larger than R is the same as the fraction of this smoothed density field that lies above the critical density for collapse:

$$F_{col}(R) = \int_{\delta_{crit}}^\infty d\delta_R \frac{1}{\sqrt{2\pi}\,\sigma(R)} \exp\left[-\frac{\delta_R^2}{2\,\sigma^2(R)}\right] = \frac{1}{2}\mathrm{erfc}\left(\frac{\delta_{crit}}{\sqrt{2}\,\sigma}\right) \tag{1.18}$$

We are primarily interested in the formation of structures capable of hosting galaxies. This means that we only consider haloes larger than some minimum radius (or effectively mass) for galaxy formation R_{gal}

$$F_{col} = \mathrm{erfc}\left(\frac{\delta_{crit}}{\sqrt{2}\,\sigma_{gal}}\right) \tag{1.19}$$

where we have multiplied by an ad hoc factor of two, which may be derived more rigorously in the extended Press-Schechter formalism, to account for that fact that δ may be negative. If we then only wish to consider haloes below some maximum radius R in a region of mean overdensity $\delta(z)$, the situation is entirely analogous and we obtain

$$F_{\rm col}(\delta, R, z) = \mathrm{erfc}\left(\frac{\delta_{\rm c} - \delta(z)}{\sqrt{2[\sigma^2_{\rm gal} - \sigma^2(R)]}}\right), \tag{1.20}$$

which gives a field of collapsed structure on any scale, from the initial density perturbations alone.

1.3 The Epoch of Reionization (EoR)

The formation of dark matter haloes large enough to facilitate galaxy formation heralded the end of the cosmic dark ages (Rees, 2000). The first stars and galaxies produced UV photons capable of ionizing the neutral hydrogen left behind by the recombination era. The subsequent change in the ionization state of the hydrogen in the IGM from being completely neutral to highly ionized is known as the epoch of hydrogen reionization.

1.3.1 THE SOURCES BEHIND REIONIZATION

The EoR is of fundamental interest, as it points towards when and how the first sources of light formed. However, before we can pinpoint the when, we must have some understanding of the nature of the first ionizing sources, as different sources dramatically change the topology and timescale of reionization. Suggested candidates include galaxies, quasars, early metal-free stars, and even primordial black holes. Amongst these, quasars are deemed unlikely as their number density drops too rapidly towards high redshift (Pei, 1995; Boyle et al., 2000; Richards et al., 2005), to sustain the UV flux required to reionize hydrogen. Meanwhile, early populations of massive stars, and the black holes they give rise to, are probably too short lived to have maintained an ionized IGM to the present day. Therefore, the dominant contribution to the ionizing background required during the EoR is expected to come from star forming galaxies. For the remainder of this thesis, we will only consider such sources as the catalysts of hydrogen reionization. The consideration of other source populations, while desirable, is beyond the scope of our analysis.

1.3.2 THE TOPOLOGY OF REIONIZATION

Once we assume that the ionizing photons responsible for reionization are produced by the UV light from galaxies, both analytical (Madau et al., 1999; Miralda-Escudé et al., 2000; Furlanetto & Oh, 2005) and numerical (Gnedin, 2000; Razoumov et al., 2002; Sokasian et al., 2003; Ciardi et al., 2003; Iliev et al., 2006) models predict an inhomogenous and extended EoR, with three distinct phases.

The first, or pre-overlap, phase begins slowly with photons from individual ionizing sources forming isolated bubbles of ionized hydrogen in a predominantly neutral medium. Evolution in this phase is relatively easy to trace as the change in proper volume (V_p) of individual bubbles is determined only by the balance between ionizations and recombinations. Since new ionizations are directly related to the number of ionizing photons produced N_γ and recombinations only depend on the square of the neutral hydrogen number density $n_{\rm H}$, we may write

$$\frac{d}{dt}(n_{\rm H}V_{\rm p}) = \frac{dN_\gamma}{dt} - \langle n_{\rm H}^2\rangle \alpha_{\rm B} V_p \tag{1.21}$$

where the recombination rate is proportional to the case B recombination coefficient $\alpha_{\rm B}$, which allows for on the spot re-absorption of photons emitted by recombination. Re-expressing this in terms of the co-moving volume $V = V_p a^{-3}$, we obtain

$$\frac{dV}{dt} = \frac{1}{\langle n_{\rm H}\rangle}\frac{dN_\gamma}{dt} - \langle n_{\rm H}\rangle \alpha_{\rm B} C a^{-3} V \tag{1.22}$$

where we have introduced a clumping factor $C \equiv \frac{\langle n_{\rm H}^2 \rangle}{\langle n_{\rm H} \rangle^2}$ to model the variance or non-uniformity of hydrogen density inside the bubble. This relationship tells us that the spherical H II regions created in the first stages of reionization expand outwards until a balance is reached between ionizations and recombinations, which typically occurs at around 20 times the virial radius of the original halo.

As ionizing sources become more numerous and H II bubbles increase in size, they begin to overlap and the flux from individual sources combine. This ushers in the much more rapid overlap phase of reionization. Tracing the ionization state of the IGM during this era is much more difficult. However me may estimate it by first considering a universe of volume V_t consisting of isolated ionized spheres of volume V_i, and calculating the total ionized volume using equation 1.22

$$\frac{d}{dt}\sum_i \frac{V_i}{V_t} = \frac{1}{\langle n_{\rm H} \rangle}\frac{d}{dt}\sum_i \frac{N_\gamma^i}{V_t} - \langle n_{\rm H} \rangle \alpha_{\rm B} C a^{-3} \sum_i \frac{V_i}{V_t} \tag{1.23}$$

Recognizing $\sum_i \frac{V_i}{V_t}$ as a proxy for the filling factor of ionized hydrogen Q and $\sum_i \frac{N_\gamma^i}{V_t}$ as the density of ionizing photons n_γ

$$\frac{dQ}{dt} = \frac{1}{\langle n_{\rm H} \rangle}\frac{dn_\gamma}{dt} - \langle n_{\rm H} \rangle \alpha_{\rm B} C a^{-3} Q \tag{1.24}$$

A final simplification arises from the consideration that $\frac{n_\gamma}{\langle n_{\rm H} \rangle}$ is the number of ionizing photons per hydrogen atom or $\frac{1}{0.76}$ of the number of ionizing photons per baryon. If we introduce a constant $N_{\rm ion} \equiv$ number of ionizing photons per baryon in galaxies and recall that equation 1.20 gives the fraction of baryons in collapsed structures or galaxies, we have

$$\frac{n_\gamma}{\langle n_{\rm H} \rangle} = \frac{N_{\rm ion} F_{col}}{0.76} \tag{1.25}$$

This leaves us with

$$\frac{dQ}{dt} = \frac{N_{\rm ion}}{0.76}\frac{dF_{col}}{dt} - \langle n_{\rm H} \rangle \alpha_{\rm B} C a^{-3} Q \tag{1.26}$$

to describe the evolution of the ionization state of the universe into the overlap regime. This picture does not capture the topology of overlapping sources, and furthermore hides much of the baryonic physics in the catch-all parameter $N_{\rm ion}$. Nevertheless, it remains a good first order approximation to the behaviour of ionization fraction during the overlap phase.

The final stage of the EoR involves the reionization of the remaining high density, self-shielded regions of neutral hydrogen, which are gradually destroyed by an increasingly uniform UV background. This is the stage of least interest to us, as it carries little

information about the sources that caused reionization. Instead, in this thesis we will focus on trying to pinpoint the timescale of the overlap phase.

1.4 Observational Probes of the EoR

The discussion to this point should paint a picture of a universe that is relatively well understood at early times, but becomes more obscured as its complexity grows. We may accurately reconstruct the linear growth immediately following the recombination epoch. However, there is a great deal of uncertainty behind the physics governing non-linear gravitational collapse and the formation of stars and galaxies. In particular, it is very difficult to reconstruct analytically the reionization of cosmic hydrogen by the first sources.

It is therefore unsurprising that, in attempting to understand the EoR, we must turn instead to observation. This, however, presents its own difficulties. Most prominent amongst these is the fact that the presence of neutral hydrogen prior to reionization makes it very difficult to see beyond its very end. Neutral hydrogen absorbs and scatters photons with the energy $E = 10.2eV$ required to excite an electron to its first excited state. Since more energetic photons will be redshifted to this energy as they travel towards us, they will be scattered by any neutral hydrogen in their path. This means that for sources emitting prior to the end of the EoR, a large portion of their spectrum blueward of the Lyman-α energy will be absorbed. It is therefore exceptionally difficult to directly see the sources that caused reionization. Instead, observations of the EoR must either focus on its final stages, or else look for a more indirect imprint of reionization.

1.4.1 GUNN-PETERSON TROUGH

The most direct probe of reionization comes from the absorption of Lyman-α photons from distant quasars. Quasars, or active galactic nuclei (AGN), are rare and extremely bright sources of electromagnetic radiation formed by accretion of material onto a super-massive black hole. The super-heated discs of material accreting onto the black hole emit blackbody radiation, which peaks in the UV close to Lyman-α. This means that quasars are both bright enough to be seen at great distances, at least $z \sim 7$, and have a broad enough UV spectrum to emit photons both longward and shortward of the Lyman-α line.

The spectrum observed from distant quasars therefore consists of two parts. Photons that are not energetic enough, in the quasar rest frame, to excite electrons in hydrogen travel to us unimpeded by the presence of neutral hydrogen. Meanwhile, light that is more energetic than $10.2eV$ is absorbed, as described above, by any neutral hydrogen present when it is redshifted into Lyman-α resonance. If the EoR is complete at the time of quasar emission, neutral hydrogen is only present in rare, dense self-shielded regions

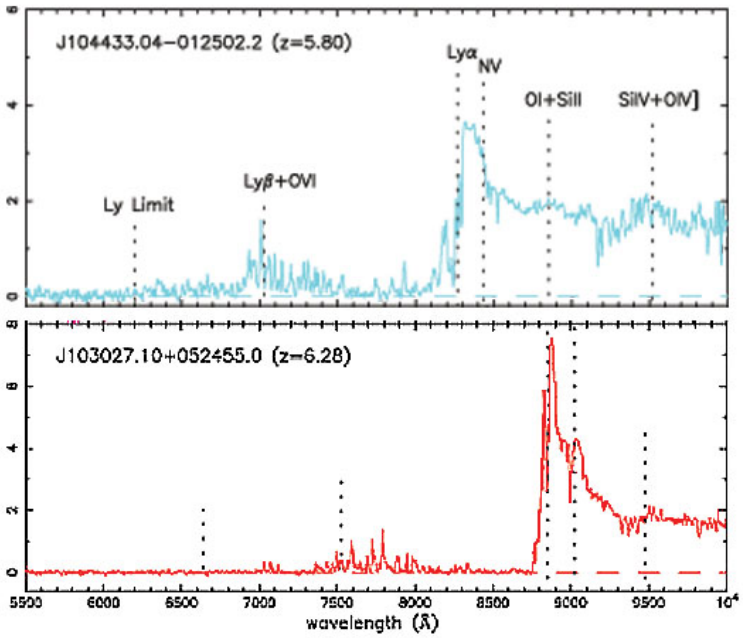

FIGURE 1.1: High resolution spectra of two quasars at $z > 5.5$. Shortward of the redshifted rest-frame Lyman-α wavelength we see clear signs of absorption in both quasars. At $z = 6.28$, this manifests itself as a Gunn-Peterson Trough between 8000 and 8700AA corresponding to saturated absorption for redshifts in the range $5.6 < z < 6.2$. Meanwhile, at $z = 5.80$ we observe a Lyman-α forest of absorption troughs due to absorbers along the line of sight. This is used to infer that by $z \approx 6$ reionization has ended. Figure taken from Becker et al. (2001).

like large galaxy clusters and so absorption only occurs infrequently. This results in a Lyman-α forest of absorption troughs observed in the quasar spectrum. On the other hand, if the EoR is ongoing, neutral hydrogen is present virtually everywhere and so all light at the correct frequency is absorbed. This creates a region of saturated absorption in the spectrum referred to as a Gunn-Peterson (GP) trough.

An example of Lyman-α GP troughs observed in the spectra of two quasars at $z > 5.5$ is shown in figure 1.1. The absence of the trough in the spectra at $z < 6$ indicates that the neutral hydrogen fraction in the IGM surrounding the quasar is sufficiently small by this epoch (Fan et al., 2006). Meanwhile, the detection of a GP trough at $z > 6$ indicates that the neutral hydrogen fraction is large enough at that redshift to fully absorb the quasar flux (Becker et al., 2001; Fan et al., 2006).

The neutral fraction that corresponds to this complete suppresion can be calculated by noting that the optical depth to a quasar at redshift z_q, in terms of the neutral hydrogen density $n_{\rm H}$ and the Lyman-α cross-section σ_α is

$$\tau_{\rm GP} = \sigma_\alpha \int_0^{z_q} n_{\rm H}(z) \frac{dl}{dz} dz \tag{1.27}$$

In the matter dominated era, $z \geq 2$, the proper line element $\frac{dl}{dz}$ may be expressed as

$$\frac{dl}{dz} = -\frac{c}{H(z)(1+z)} \approx -\frac{c}{H_0 {\Omega_m}^{\frac{1}{2}} (1+z)^{\frac{3}{2}}} \tag{1.28}$$

so that the Gunn-Peterson optical depth is

$$\tau_{\rm GP} \approx \frac{\sigma_\alpha c n_{\rm H}(z_q)}{H_0 {\Omega_m}^{\frac{1}{2}} (1+z_q)^{\frac{3}{2}}} \tag{1.29}$$

If we substitute for fiducial values in a ΛCDM universe

$$\tau_{\rm GP} \approx 4.28 \times 10^5 (1-Q)(1+\delta)(\frac{1+z_q}{7})^{\frac{3}{2}} \tag{1.30}$$

It is clear from this result that the absence of a Gunn-Peterson trough ($\tau_{\rm GP} < 1$), indicates a highly ionized IGM, since at $z \approx 6$ we require a neutral hydrogen fraction of $1 - Q \lesssim 10^{-5}$ to observe this. Consequently, a robust lower limit to the end of the reionization epoch is $z \approx 6$; below this redshift the IGM appears to be highly ionized everywhere.

The flip side of this is that the GP optical depth is highly insensitive to the exact ionization state of intergalactic hydrogen, since all neutral fractions of order $(1 - Q) \approx 10^{-4}$ or more will result in saturated absorption. The GP trough therefore only tells us a redshift by which reionization must be complete, and does not inform us of when the more interesting overlap phase occurs.

1.4.2 THOMSON OPTICAL DEPTH

Instead of using absorption by neutral hydrogen, we can probe deeper into the EoR by studying the density of free electrons released by reionization. CMB photons travel towards us from the recombination era and along their path are scattered and polarised by free electrons. This has the effect of correlating polarization and brightness anisotropies in the CMB signal. Measuring the strength of this correlation yields the optical depth to electron scattering, $\tau_{\rm CMB} = 0.088 \pm 0.015$ (Komatsu et al. 2011), according to the latest WMAP observations. This is then related to the integrated electron, or equivalently ionized hydrogen, density by

$$\tau_{\rm CMB} = \int_0^{z_{\rm CMB}} c\frac{dt}{dz} Q(z)\,(1 + f_{\rm He}(z))\,n_{\rm H}(z)\sigma_{\rm T} dz, \tag{1.31}$$

where $\sigma_{\rm T}$ is the Thomson scattering cross-section, and $f_{\rm He}$ is a correction factor due to the presence of ionised helium.

The problem with this quantity as a tracer of the EoR is that it is only an integrated measure and so does not distinguish between different ionization histories. If we assume reionization is instantaneous then we may conclude that the redshift at which overlap occurs is $z_r = 10.6 \pm 1.2$. However, it is equally possible to acheive the same optical depth for a far more extended reionization process, which only completes by $z_{\rm r} \approx 6$.

1.5 Temperature as a Probe of the EoR

The observations described above are fundamentally limited in what they can tell us about the EoR. The Gunn-Peterson trough is overly sensitive to the presence of neutral hydrogen and so can only probe the tail end of reionization. Meanwhile, the Thomson optical depth probes deeper but cannot tell us much about the timescale of reionization. The net effect is that efforts to discover when reionization occured, even when they include restrictive models, still retain an uncertainty of around $\Delta z_r \approx 4$ (Mitra et al., 2011). Furthermore, in the absence of more accurate models for reionization, or observations at $z > 6$, these uncertainties will not be improved upon.

One possible solution to this problem lies in measuring the secondary thermal imprint left behind by hydrogen reionization. The thermal evolution of a patch of IGM is governed by the balance between ionization heating, recombination cooling and adiabatic cooling due to the expansion of the universe

$$\frac{dT}{dt} \approx \frac{(\gamma - 1)\mu m_{\rm p}}{k_{\rm B}\rho}\left[G(t) - \Lambda(t, n_{\rm i})\right] - 2H(t)T, \tag{1.32}$$

where $\gamma = \frac{5}{3}$, and G and Λ are the total photo-heating and cooling rates per unit volume, respectively. During any reionization event, the first of these terms dominates, heating

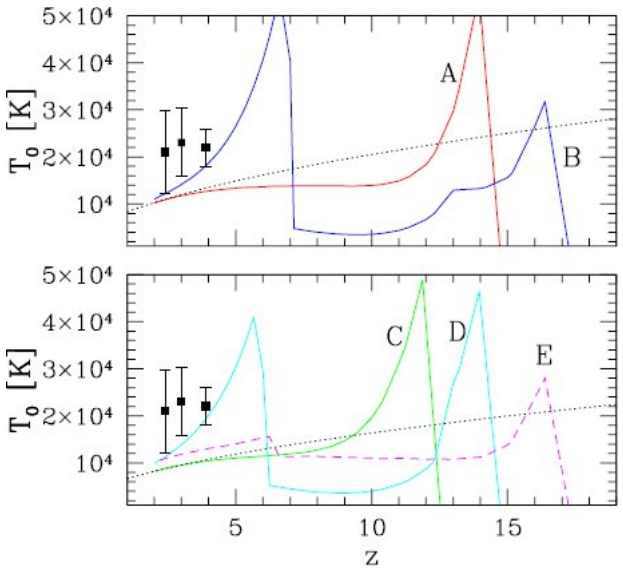

FIGURE 1.2: Thermal evolution with redshift for a number of different reionization scenarios. For comparison, observed constraints on the IGM temperature at $z = 2 - 4$ are also shown (Black squares). *Upper Panel:* Early and late reionization scenarios assuming that helium is doubly ionized at the same time as hydrogen. *Lower Panel:* Similar results this time only allowing sources to singly ionize helium. In both cases, a heating episode due to reionization at $z \sim 6 - 7$ is required to heat the IGM sufficiently to match constraints. Figure taken from Hui & Haiman (2003)

the IGM by tens of thousands of degrees. Subsequently, ionizations and recombinations reach an equilibrium and thermal evolution is driven by adiabatic cooling. This is significant, since adiabatic cooling occurs on a timescale comparable with the Hubble time or the age of the universe. Therefore, the heating caused by reionization remains long after the EoR is complete.

Using the measured IGM temperature to probe the EoR is then quite a simple idea. Assuming we can accurately model the heating caused by reionization, measurements of temperature tell us when the overlap phase, which contributes the bulk of the heating, occurs. If the universe was reionized late, adiabatic cooling of the gas cannot overcome the photo-ionization heating, and the IGM might reach too high a temperature at low redshifts compared to observations. Conversely, if it was reionized early, the opposite would hold true and the temperature would be too low to match observations.

1.5.1 PREVIOUS WORK

This idea is not new and Miralde-Escude & Rees (1994); Hui & Gnedin (1997); Haehnelt & Steinmetz (1998); Schaye et al. (2000); Theuns et al. (2002); Hui & Haiman (2003)

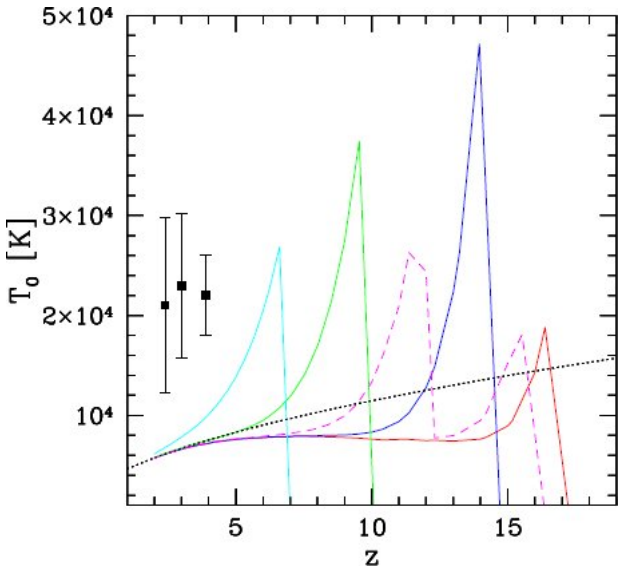

FIGURE 1.3: Thermal evolution with redshift for a number of different overlap redshifts. Shown in black is the thermal asymptote, to which all scenarios prior to $z_{\rm r} \approx 8.0$ converge by $z = 4$. Figure taken from Hui & Haiman (2003).

have all used IGM measurements at $z = 2 - 4$ to provide limits on the EoR. Figure 1.2 shows results from Hui & Haiman (2003) comparing different reionization scenarios on the basis of their thermal history. They show the evolution in temperature of a patch of mean density IGM, which is reionized instantaneously. It is clear from their results that, irrespective of the assumptions made concerning the sources causing reionization, some reionization and heating episode is required at low redshift $z < 10$ in order to match the relatively high observed temperatures. These results are then used to infer an overlap redshift of $z_{\rm r} < 10$.

However, their analysis, and all those preceding it, suffer from a number of drawbacks. Primarily, their assumption of instantaneous reionization, does not capture the physics of the growth and overlap of ionizing bubbles, as described in Section 1.3.2. Similarly, by only calculating for a mean density IGM, they ignore the density dependence of both ionization in Equation 1.23 and heating in Equation 1.32. Their model only imprints the effects of extended reionization and varying density as a posteriori adjustments to the simple scenarios shown in Figure 1.2. They therefore, do not necessarily capture the correct variance, or even mean, of the IGM temperature distribution.

A secondary problem arises from comparisons to temperature measurements at $z = 2 - 4$. As mentioned in Section 1.3.1, the quasar density peaks around these redshifts, leading to a change in the background spectrum from being galaxy-dominated to quasar-dominated. There is strong evidence to suggest that this leads to an epoch of helium reionization at this time (Madau & Meiksin 1994; Wyithe & Loeb 2003; Furlanetto &

Oh 2008), which heats the IGM above the thermal asymptote reached following hydrogen reionisaton. Therefore, it becomes difficult to disentangle the EoR signal from the helium heating signal.

On top of this, the thermal imprint of reionization does not last forever, meaning that relatively low redshift measurements do not retain a memory of events deep into the EoR. Figure 1.3 shows the effect of different reionization times on the low redshift thermal record. All reionization scenarios prior to $z_{\rm r} \approx 8$ converge to the same thermal asymptote, which only depends on the ionizing spectrum by $z = 4$. Therefore, higher redshift measurements are necessary to both avoid the helium heating epoch and differentiate different overlap redshifts.

To remedy this, in a more recent study Bolton et al. (2010) have used the temperature observed around a quasar at $z \approx 6$ to infer a local reionization redshift. However, their constraints still suffered from using an instantaneous model of reionization, and only looked at the quasar proximity zone. Our objective here is to extend their analysis to the general IGM, with the use of 7 new observations around quasars in the range $z \approx 5.5 - 6.5$ (Bolton et al., 2011). Specifically, by modelling the inhomogeneous reionisation and photo-heating of intergalactic hydrogen by stellar sources, as well as any subsequent photo-heating by quasars themselves, we calculate the proximity zone temperature as a function of spatial position and reionisation redshift. A comparison of our model with the observational data then allows us to constrain the redshift at which reionisation completed. We seek constraints on the EoR that are as robust as possible, correctly accounting for inhomogeneous reionization, the density dependence of temperature measurements and a wide range of modelling uncertainties.

1.6 Thesis Outline

The thermal imprint of reionization represents a powerful means of probing the EoR and correspondingly also the first galaxies in the Universe. Our aim through this thesis is to better understand the origins of this imprint and subsequently answer the question:

- What was the timescale of the EoR, and more specifically when did the overlap phase of reionization occur?

The thesis is organised as follows. We begin in §2 by introducing our semi-numerical model of reionisation, and proceed in §3 to give a more detailed description of the modelling of ionising sources. Predicted temperatures from the model for different reionisation scenarios are then described in §4 and compared to the Bolton et al. (2011) quasar temperature measurements. Our constraints on reionisation history are then discussed in §5, where we also assess the prospects for improving on these constraints in the future using additional quasar sight-lines. Conclusions and further directions are then presented in §6.

Chapter 2

Semi-Numerical Reionisation Model

Our model of inhomogeneous hydrogen reionisation simulates both the evolving ionisation state of the IGM and its thermal history. The former is calculated using the semi-numerical model developed by Wyithe & Loeb (2007) and Geil & Wyithe (2008) (see also Zahn et al. 2007; Mesinger & Furlanetto 2007; Choudhury et al. 2009; Thomas et al. 2009 for similar approaches). The ionisation state derived from this model is then used to evaluate both the ionising flux and the mean free path at the Lyman Limit, and to infer a temperature distribution for the IGM.

2.1 Construction of Density Field

We simulate the IGM inside a periodic, comoving grid of side-length $L = 100\,h^{-1}\,\mathrm{Mpc}$, containing $N = 256$ voxels per side-length. The linear overdensity field $\delta(\mathbf{x})$ on this grid is drawn from a random gaussian distribution, with a power spectrum defined by equation 1.14 and normalized using σ_8. Numerically, this procedure is carried out by laying down a cubic grid of size N^3 and approximating the continuous Fourier relationship between $\delta(\mathbf{x})$ and the Fourier space density contrast $\hat{\delta}(\mathbf{k})$ with its discrete form,

$$\hat{\delta}(\mathbf{k}) = \frac{V}{N^3} \sum_x \delta(\mathbf{x}) e^{-i\mathbf{k}\cdot\mathbf{x}} \tag{2.1}$$

Each Fourier density mode is calculated by sampling the power spectrum at each of a finite set of wavenumbers $k = (l, m, n)k_0$, where $l, m, n \in \{-\frac{N}{2}+1, \frac{N}{2}+2, ..., \frac{N}{2}\}$ and $k_0 = \frac{2\pi}{L}$. In order to realize the Gaussianity of $\delta(\mathbf{x})$ we draw both the real and complex components of $\hat{\delta}(\mathbf{k})$ from a zero-mean normal distribution with variance $\sigma^2 = \frac{P(k)V}{2}$. Furthermore, we enforce Hermiticity upon $\hat{\delta}(\mathbf{k})$ to ensure $\delta(\mathbf{x})$ is real. All seven vertices corresponding to the positive frequency Nyquist modes must be real, and in order to

produce a zero-mean density field the DC mode $\hat{\delta}(\mathbf{k} = \mathbf{0})$ is set to zero. The three-dimensional inverse Fourier transform of $\hat{\delta}(\mathbf{k})$ gives an Eulerian realization of $\delta(\mathbf{x})$ filtered on a scale $\Delta = \frac{L}{N}$ (Sirko, 2005).

2.2 Ionisation model

The calculations detailing the evolution of ionisation structure from the dark matter structure detailed above are described in Geil & Wyithe (2008). Briefly, the model attempts to characterise the relationship between the formation rate of virialised haloes and the ionization rate of the surrounding universe. Modelling this relationshop is non-trivial as it depends on various internal parameters (which may vary with galaxy mass), such as the fraction of gas within galaxies that is converted into stars and accreting black holes, the spectrum of the ionizing radiation, and the escape fraction of ionising photons from the galactic halo and its immediate infall region [see Loeb (2006) for a review]. The process of reionization itself also contains several layers of feedback, which modify these parameters. Radiative feedback heats the IGM and results in the suppression of low-mass galaxy formation (Efstathiou et al., 1992; Thoul et al., 1996; Quinn et al., 1996; Dijkstra et al., 2004). This delays the completion of reionization by lowering the local star formation rate, but the effect is counteracted in overdense regions by the biased formation of massive galaxies.

The model of Geil & Wyithe (2008) describes all of these dependencies using the simple ionization model of equation 1.24. Therefore, the majority of the physics is hidden in the redshift-dependent parameter $N_{\rm ion}(z)$, the modelling of which will be described in greater detail in Chapter 3. Only the reionization feedback is modelled differently as an increase in the minimum galaxy mass in ionized regions from $M_{\rm min}$ to $M_{\rm ion}$. We assume $M_{\rm min}$ to correspond to a virial temperature of 10^4 K, representing the hydrogen cooling threshold, and $M_{\rm ion}$ to correspond to a virial temperature of 10^5 K, representing the mass below which infall is suppressed from an ionized IGM (Dijkstra et al., 2004). With these two strictures, we evaluate the ionisation fraction $Q_{\delta_R,R}$ of a spherical region of scale R around a given voxel at redshift z as

$$\begin{aligned}\frac{dQ_{\delta_R,R}}{dt} &= \frac{N_{\rm ion}}{0.76}\left[Q_{\delta_R,R}\frac{dF_{\rm col}(\delta_R,R,z,M_{\rm ion})}{dt}\right.\\ &+ \left.(1-Q_{\delta_R,R})\,\frac{dF_{\rm col}(\delta_R,R,z,M_{\rm min})}{dt}\right]\\ &- \alpha_{\rm B}Cn_{\rm H}^0\left[1+\delta_R\frac{D_1(z)}{D_1(z_{\rm obs})}\right](1+z)^3\,Q_{\delta_R,R},\end{aligned} \tag{2.2}$$

where δ_R is the region's over-density, C is the subgrid clumping factor and $F_{\rm col}(\delta_R, R, z, M_{\rm gal})$

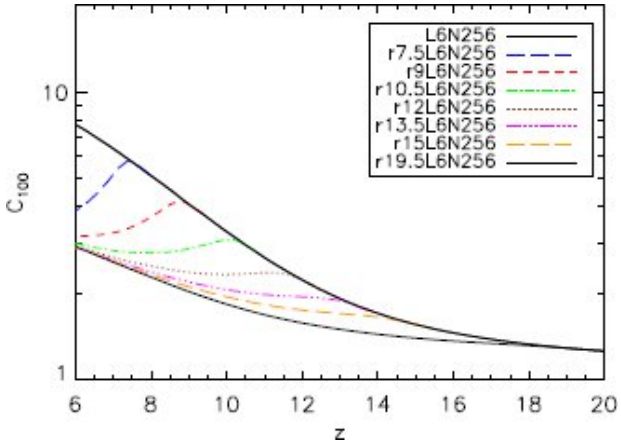

FIGURE 2.1: Evolution of the clumping factor C_{100} for different reionization redshifts $z_{\rm r}$, as indicated with the first number in the legends. The black solid lines show the cases of no photo-heating (upper curve) and photoheating at $z_{\rm r} = 20.0$ (lower curve) repsectively. We observe that C_{100}, in all simulations evolves from the no heating value towards the clumping factor obtained in the early reionization simulation. Therefore, the clumping factor remains relatively constant through reionization and at $z = 6$, is $C_{100} \approx 3$ irrespective of $z_{\rm r}$. Figure taken from Pawlik et al. (2009)

is the fraction of baryons in galaxies as defined by equation 1.20, with a minimum galactic mass $M_{\rm gal} = M(R_{\rm gal})$.

In addition to $N_{\rm ion}(z)$, the clumping factor adds a second uncertainty to our modelling of reionization. Since it effectively modulates the recombination rate in Equation 2.2 and subsequently also the recombination cooling, C can have a significant impact on our modelling as it acts to both slow down reionization and increase the overall photoheating. However, its exact value, and its evolution with redshift, is unknown as it is essentially a measure of how non-linear the density field becomes. Furthermore, various feedback mechanisms, including photoheating from reionization can add pressure, which smooths over small-scale fluctuations, and dramatically alter C. Therefore, to understand the clumping factor, we must turn to hydrodynamical simulations, which model both non-linear gravitational collapse and photo-heating. Figure 2.1 shows the results from Pawlik et al. (2009), who used hydrodynamical simulations to model the clumping factor for different reionization scenarios. In each case, we see that while C evolves prior to reionization with the collapse of haloes, once photoheating begins pressure smoothing keeps it relatively constant at $C \approx 3 - 4$. Therefore, throughout this work we shall assume $C = 3$, broadly consistent with these results and others from recent hydrodynamical simulations (Pawlik et al. 2009; Raicević & Theuns 2010).

Once C and $N_{\rm ion}(z)$ are set, Equation 2.2 is solved at every voxel on a range of scales from L to L/N at logarithmic intervals of width $\Delta R/R = 0.1$. A voxel is then

deemed to be ionised if it lies inside a region for which $Q_{\delta_R,R} > 1$ on any scale R. By repeating this procedure at successive redshifts, we obtain our ionisation field as a function of z.

2.3 The ionising emissivity

In order to compute the heating of the IGM, we must next obtain the ionising emissivity in each voxel of our simulation. We simulate the ionisation field at 30 regular redshift intervals between an initial redshift, z_0, and the reionisation redshift, z_r. These are, respectively, the redshifts corresponding to $Q = 0.01$ and $Q = 1.0$, where $Q = Q_{\delta_R,R}$ for the case where equation (2.2) is solved at mean density and $R \to \infty$. At each interval, if a voxel is flagged as ionised, we compute the emission rate of ionising photons per baryon. This is given by the product of N_ion and the collapsed fraction above a minimum halo mass, M_ion, where we use the minimum mass in ionised regions since the majority of ionising photons come from ionised regions. We may then relate this to the the photon emissivity ($\dot{N}_\gamma$) in proper units of photons per $\mathrm{cm}^{-3}\,\mathrm{s}^{-1}$, by multiplying by the proper baryon density

$$\dot{N}_\gamma = \frac{\rho_\mathrm{c}\Omega_\mathrm{b}(1+z)^3(1+\delta_\lambda)N_\mathrm{ion}}{\mu m_\mathrm{p}} \frac{dF_\mathrm{col}(\delta_\lambda, \lambda_\mathrm{HI}, z, M_\mathrm{ion})}{dt}, \tag{2.3}$$

where ρ_c is the present day critical density, m_p is a proton mass and μ is the mean molecular weight, which in a region of singly ionized helium and hydrogen is given by $\mu = 0.62$. In this instance, the smoothing scale used to calculate the collapsed fraction gives an estimate of the total volume through which ionising photons may travel. It is therefore given by the mean free path at the Lyman limit (λ_HI), which pre-overlap is set by the ionised bubble radius and post-overlap is set by the distance between Lyman Limits systems.

The ionising emissivity ϵ_ν, (in units of $\mathrm{erg}\,\mathrm{s}^{-1}\,\mathrm{cm}^{-3}\,\mathrm{Hz}^{-1}$) above the Lyman Limit frequency ν_HI is calculated from this by integrating over all photon energies

$$\dot{N}_\gamma = \int_{\nu_\mathrm{HI}}^{\infty} \frac{\epsilon_\nu}{h_\mathrm{p}\nu}\, d\nu, \tag{2.4}$$

where we adopt a simple power law spectrum

$$\epsilon_\nu = \left(\frac{\nu}{\nu_\mathrm{HI}}\right)^{-\alpha} \times \begin{cases} \epsilon_\mathrm{HI} & (\nu_\mathrm{HI} \leq \nu < \nu_\mathrm{HeII}) \\ 0 & (\nu_\mathrm{HeII} \leq \nu) \end{cases} \tag{2.5}$$

Here ϵ_HI is the emissivity at the hydrogen Lyman limit. Below the He II ionisation edge, we take a spectral index of $\alpha = 3$ characteristic of soft, population II stellar sources (*e.g.* Hui & Haiman 2003; Furlanetto & Oh 2009). Above ν_HeII, the spectrum is zero in

order to enforce the requirement that there be no significant stellar ionisation of He II. This is necessary for consistency with our semi-numerical reionisation model which only traces the propagation of hydrogen ionisation fronts, and so cannot predict the larger, extended He III fronts resulting from harder He II ionising photons. On the other hand this is not an unrealistic requirement, since the double reionisation of helium is thought to be delayed until $z \sim 3$ when the number density of quasars is at its peak (Madau & Meiksin 1994; Wyithe & Loeb 2003; Furlanetto & Oh 2008). Nevertheless, this assumption rules out the consideration of more exotic ionisation models involving early populations of quasars or Population-III sources, which could produce different thermal histories. More detailed modelling, which accounts for doubly ionised helium remains a work for the future. In this work, we therefore consider *hydrogen reionisation by population-II stellar sources only*.

2.4 The ionising background specific intensity

Having found the intrinsic emissivity, the specific intensity, J_ν, at each voxel may then be calculated by accounting for the propagation and attenuation of radiation. This is a complicated calculation since, in general, it depends on the topology of H II regions around each point in the simulation and the distribution of Lyman limit systems. A full numerical evaluation therefore requires radiative transfer, which is not included in our model. Fortunately, the long-term thermal evolution (for timescales longer than the local photo-ionisation timescale) is relatively insensitive to the exact amplitude of J_ν, and instead depends primarily on the spectral shape of the ionising radiation (Hui & Haiman 2003; Bolton et al. 2009). Therefore, to estimate the specific intensity we make the simplifying assumption that the mean free path is much smaller than the horizon scale, and use the local source approximation (e.g. Faucher-Giguère et al. 2009). We compute the mean free path in two regimes, prior to and following the overlap of H II regions.

2.4.1 THE PRE-OVERLAP MEAN FREE PATH

Prior to overlap, the mean free path is set by the size of H II bubbles (Gnedin & Fan 2006), and may therefore be found by partitioning the ionisation field into approximately spherical H II regions. This is not a straightforward process, since as we proceed towards the overlap phase ionized bubbles will change from their initially spherical shape to more complex topologies. In particular, the overlap phase will create bridging regions between adjacent bubbles, which we do not wish to identify as being part of the much larger bubbles. The upper left panel of Figure 2.2 shows an example of this prior to the overlap phase, when the IGM has a filling factor of $Q \approx 0.1$. Although it is slightly hard to discern, given that we are looking at a 2D slice through a 3D simulation box, we note that the system of small bubbles in the upper middle section of the ioniza-

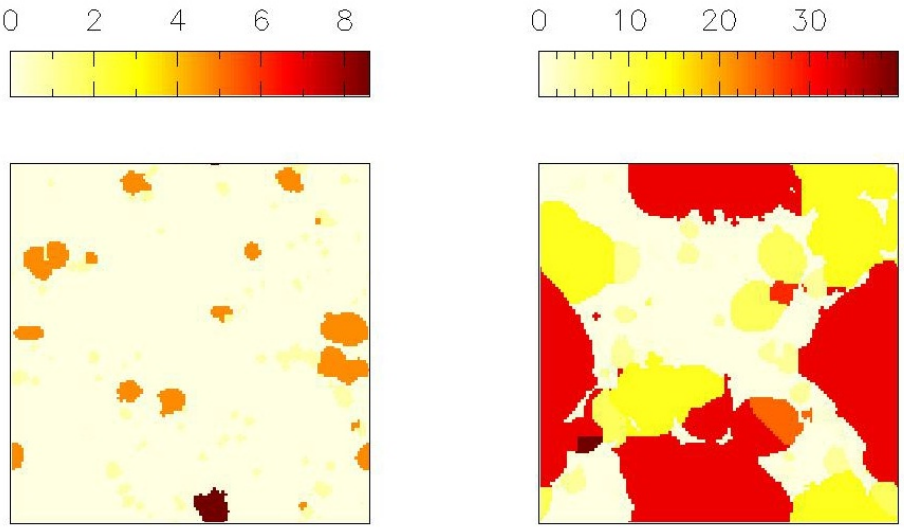

FIGURE 2.2: 2D slices through the ionization field showing bubble size distributions at filling factors of $Q \approx 0.1$ (left) and $Q \approx 0.5$ (right) respectively. The differing colors indicate the comoving radii in Mpc of approximately spherical bubbles.

tion field are linked by small ionized corridors or bridges, but are distinct in terms of the mean free path. We therefore employ the following algorithm to formally separate such bubbles:

- We begin by smoothing the ionization field with a spherical top hat on a given scale R so as to eliminate bridging regions of that size. This leaves behind a field of ionized pixels, which must be part of spherical regions with radius greater than R.

- To find the bubbles to which these ionized voxels belong, we use a friend-of-friends (FOF) bubble finding algorithm. Essentially this consists of determining whether an ionized voxel is adjacent to any others, where adjacency is determined by whether or not the cubic faces of the voxels touch. If pixels are deemed to be adjacent, they are added to the same bubble, which gives us a list of distinct bubbles and the voxels that belong to them.

- The smoothing process not only eliminates bridging regions, it also eliminates voxels on the boundaries of much larger ionized bubbles. To determine which bubbles these boundary voxels belong to, we must subsequently run a FOF algorithm on the unsmoothed ionized field. However, in this case care must be taken, since the algorithm merges bubbles that are distinct at a scale R. Therefore, we

run the FOF procedure at each bubble simultaneously proceeding radially outward from the bubble boundary. Then, each voxel is assigned to a unique bubble at this scale, and that bubble is the one whose smoothed boundary is closest.

- Once all bubbles are found at a scale R, the procedure is repeated over a range of different scales so as to eliminate bridging regions of different sizes. In this case, the smoothing scale is increased in linear steps of $\Delta R = 5R_{\rm min}$ as the ionizing intensity in Equation 2.7 scales linearly with the mean free path.

- Finally, each voxel will be assigned a bubble size at each scale. Its nominal bubble size is then the minimum of all calculated sizes. The justification for this is that if a bridging region is not smoothed over at some scale, it can only be assigned to a much larger bubble and not a smaller one. Therefore, the best approximation of the region size is given by the smallest calculated radius.

Figure 2.2 shows the results of this algorithm when applied to our ionization field both prior to (upper left) and during (upper right) the overlap phase. Before overlap, when the bubbles are still approximately spherical, we succeed in differentiating between bubbles that are virtually discontiguous. However, once the filling factor becomes too large our procedure begins to break down, effectively separating elongated elliptical bubbles into different regions. Nevertheless, with this algorithm the spherical approximation remains valid to a filling factor of around $Q \approx 0.5$.

2.4.2 THE POST-OVERLAP MEAN FREE PATH

In the post-overlap case, the IGM is fully ionised and the mean free path of H I ionising photons is constrained by the abundance of Lyman limit systems rather than the sizes of H II regions. In this instance, we employ a fit to the mean-free-path at the Lyman limit in proper Mpc, taken from Songaila & Cowie (2010):

$$\lambda_{\rm HI} = \frac{88.6}{\Gamma(2-\beta)}\left(\frac{1+z}{4.5}\right)^{-4.44} {\rm Mpc}, \tag{2.6}$$

where Γ denotes the gamma function, and β is the power law exponent of the H I column density distribution. Observationally, the exact value of this exponent is not well constrained, however throughout we take $\beta = 1.5$ (Petitjean et al. 1993). Finally, we assume that a given H II region is in the pre-overlap regime if its radius is less than $\lambda_{\rm HI}$ (i.e. the mean free path is not set by Lyman limit systems) and is in the post-overlap regime otherwise.

Adopting the local source approximation, the ionising background specific intensity in each voxel may then be approximated by

$$J_\nu \simeq \frac{1}{4\pi}\epsilon_\nu \lambda_\nu, \tag{2.7}$$

where $\lambda_\nu = \lambda_{\rm HI}(\nu/\nu_{\rm HI})^{3(\beta-1)}$. Prior to overlap $\lambda_{\rm HI}$ is fixed to the H II region size, while post overlap it is given by equation 2.6. Lastly, note that in both regimes at frequencies above the Lyman Limit, we have $J_\nu \propto \nu^{-\alpha+3(\beta-1)}$. This effectively hardens the intrinsic stellar spectrum by $\alpha \rightarrow \alpha - 1.5$, accounting for the additional heating due to filtering of the ionising radiation by discrete, Poisson distributed absorbers in the intervening IGM (e.g. Miralda-Escudé 2003; Faucher-Giguère et al. 2009).

2.5 Thermal evolution

Once the specific intensity at a given voxel is known, the photo-ionisation rates, $\Gamma_{\rm i}\,[{\rm s}^{-1}]$, and photo-heating rates, $g_{\rm i}\,[{\rm erg\,s}^{-1}]$, for $i =$ H I, He I and He II, may be calculated via:

$$\Gamma_{\rm i} = \int_{\nu_{\rm i}}^{\infty} \frac{4\pi J_\nu}{h_{\rm p}\nu}\sigma_{\rm i}(\nu)d\nu, \tag{2.8}$$

$$g_{\rm i} = \int_{\nu_{\rm i}}^{\infty} \frac{4\pi J_\nu}{h_{\rm p}\nu}h_{\rm p}(\nu-\nu_{\rm i})\sigma_{\rm i}(\nu)d\nu, \tag{2.9}$$

where $\sigma_{\rm i}(\nu)$ and $\nu_{\rm i}$ are the photoionisation cross-section and frequency of the ionisation edge for species i, and are based on the fitting functions in Verner et al. (1996). The temperature evolution is then computed by solving:

$$\frac{dT}{dt} = \frac{(\gamma-1)\mu m_{\rm p}}{k_{\rm B}\rho}\left[G(t) - \Lambda(t, n_{\rm i})\right] - 2H(t)T + \frac{T}{\mu}\frac{d\mu}{dt}, \tag{2.10}$$

where $\gamma = \frac{5}{3}$, and $G = \sum_{\rm i} n_{\rm i} g_{\rm i}$ and Λ are the total photo-heating and cooling rates per unit volume, respectively. We ignore any heating resulting from the growth of density fluctuations as this is a minimal effect throughout the short timescale of reionisation. The non-equilibrium abundances of these species are found by additionally solving three differential equations coupled to equation 2.10 (e.g. Anninos et al. 1997; Bolton & Haehnelt 2007)

$$\frac{dn_{\rm HII}}{dt} = n_{\rm HI}(\Gamma_{\rm HI} + n_{\rm e}\Gamma_{\rm eHI}) - n_{\rm HII}n_{\rm e}\alpha_{\rm HII}C \tag{2.11}$$

$$\frac{dn_{\rm HeII}}{dt} = n_{\rm HeI}(\Gamma_{\rm HeI} + n_{\rm e}\Gamma_{\rm eHeI}) + n_{\rm HeIII}n_{\rm e}\alpha_{\rm HeIII}C - n_{\rm HeII}(\Gamma_{\rm HeII} + n_{\rm e}\Gamma_{\rm eHeII} + n_{\rm e}\alpha_{\rm HeII}C) \tag{2.12}$$

$$\frac{dn_{\rm HeIII}}{dt} = n_{\rm HeII}(\Gamma_{\rm HeII} + n_{\rm e}\Gamma_{\rm eHeII}) - n_{\rm HeIII}n_{\rm e}\alpha_{\rm HeIII}C \tag{2.13}$$

with closing conditions

$$n_{\rm HI} = n_{\rm H} - n_{\rm HII} \tag{2.14}$$

$$n_{\rm HeI} = \frac{1 - 0.76}{4 \times 0.76} n_{\rm H} - n_{\rm HeII} - n_{\rm HeIII} \tag{2.15}$$

$$n_{\rm e} = n_{\rm HII} + n_{\rm HeII} + 2n_{\rm HeIII} \tag{2.16}$$

where we have assumed a uniform clumping factor of $C = 3$ for all species. The collisional ionisation rates for each species $\Gamma_{\rm ei}$, as well as all cooling rates Λ are drawn from Bolton & Haehnelt (2007), while the case-B recombination and cooling rates come from Hui & Gnedin (1997).

Our code for solving equation 2.10 follows photo-ionisation and heating, collisional ionisation, radiative cooling, Compton cooling and adiabatic cooling for six species (H I, H II, He I, He II, He III, $\rm e^-$). For reasons of numerical stability, we employ a first order implicit scheme for solving equations 2.13 and 2.10 as described in Anninos et al. (1997). This involves solving the following coupled set of recurrence relations for the density of species i, n_i^{k+1} and temperature T^{k+1} at some time $t^{k+1} = t^k + \Delta t$:

$$J_\nu^{k+1} = J_\nu(t^{k+1}) \tag{2.17}$$

$$n_i^{k+1} = n_i^k + f(n_i^{k+1}, T^{k+1}) \tag{2.18}$$

$$T^{k+1} = T^k + \frac{(\gamma - 1)\mu m_{\rm p}}{k_{\rm B}\rho} \left[G(n_i^{k+1}, t^{k+1}) - \Lambda(n_i^{k+1}, t^{k+1}) \right] \Delta t \tag{2.19}$$

$$- 2H(t^{k+1})T^{k+1} + \frac{T^{k+1}}{\mu} \Delta\mu \tag{2.20}$$

where $f(n_i^k, T^k)$ are the density gradient functions in equation 2.19. These implicit relations are solved by making initial guesses for the densities $n_i^{k+1,0} = n_i^k$ and temperature $T^{k+1,0} = T^k$. We then recursively solve the relations at a given timestep until $|n_i^{k+1,n} - n_i^{k+1,n-1}| < \epsilon$ for some pre-determined value ϵ, which determines whether or not the solution has converged. For our convergence criterion, we look only at the electron density as this is a proxy for total change in the system, and choose ϵ such that the fractional change at each timestep is less than 10^{-6}.

For reasons of efficiency, an adaptive timestepping scheme is also adopted in solving equations 2.19 and 2.20. The thermal evolution takes place on two fundamentally different time scales. During a reionization event, the short hydrogen ionization timescale, $t_{ion} = \frac{1}{\Gamma_{\rm HI}}$, dominates, however after this brief heating event we transition to a much slower cooling phase, which occurs on the hubble time scale, $t_H = \frac{1}{H(t)}$. As these scales are separated by tens of orders of magnitudes, it becomes inefficient to solve the recurrence relations with a fixed timestep. We therefore adopt an additive decrease,

multiplicative increase model of adaptive timestepping. If the convergence criterion ϵ is not met at a given timestep after a fixed number of iterations, we either take $\Delta t = t_{ion}$ or else if $\Delta t < t_{ion}$, we subtract off a fixed fraction of the photo-ionization time. On the other hand, if the criterion is met, we double Δt for the following timestep. This ensures a fast transition from the photo-ionization scale to the adaiabatic cooling scale, once the bulk of reionization is complete.

Using this prescription, we evolve the temperature of each voxel, independent of all others from an initial temperature $T_0 = 2.27(1+z)\mathrm{K}$ and an initially neutral state. We note that this effectively assumes that at each voxel, sources switch on instantaneously across the whole region and that the subsequent thermal evolution is independent of neighbouring voxels. However, as each voxel is relatively small $\mathcal{O}(\mathrm{Mpc}^3)$ and neighbouring voxels are already coupled by our simulation of reionization in 2.2, these assumptions are well justified.

Care must also be taken when assigning the density of each voxel since our ionization model only traces the linear density field and not the real density. For the higher density regions, in which non-linear collapse takes over at early times, this is not a good approximation, while for the lowest density regions, the gaussianity of the linear field leads to negative densities. Therefore, the gas density, ρ, is evaluated by mapping the normal distribution of our linear over-density field to a log-normal fit (Coles & Jones 1991), with the same total amount of matter. This approximates the real non-linear density for the majority of voxels. Whilst it does not adequately reproduce the extreme over-dense and underdense tails of the density distribution (Becker et al. 2007), its use does not represent a significant source of error since we are primarily interested in the temperature at mean density. Inaccuracies in evaluating the thermal history of the small number of regions that fall within these tails are therefore unimportant.

2.6 Inclusion of quasar heating

The final part of our model is including the effect of the quasar itself on the thermal state within its proximity zone. The model of the previous sections yields a temperature distribution over our simulation volume as a function of redshift. The ionising flux from a quasar will significantly alter this thermal state as its harder, non-thermal spectrum will also reionise He II (Bolton et al. 2010). We account for the heating effect of quasars in our semi-numerical model by augmenting the specific intensity in each voxel within the quasar proximity zone by an additional term

$$J_{\nu,\mathrm{q}} \simeq \frac{L_\nu}{(4\pi R)^2} \exp\left[-\frac{R}{\lambda_{\mathrm{HI}}}\left(\frac{\nu}{\nu_{\mathrm{HI}}}\right)^{-3(\beta-1)}\right], \tag{2.21}$$

where R is the proper distance from the quasar and $L_{\nu,\mathrm{q}} = L_{\mathrm{HI,q}}(\nu/\nu_{\mathrm{HI}})^{-\alpha_{\mathrm{q}}}$ is the quasar

ionising luminosity, again taken to be a power law spectrum with index $\alpha_{\rm q}$. There is considerable uncertainty concerning the exact value of this exponent towards high redshift. We therefore allow it to vary over the range $1.0 \leq \alpha_{\rm q} \leq 2.0$, which is consistent with recent observations of quasars at $z > 6$ (Wyithe & Bolton 2010). To compute the quasar luminosities at the Lyman limit, we take the absolute AB magnitudes from Carilli et al. (2010). This is then related to the amplitude of the luminosity density by equation 2.4. Finally, we fix the extent of the region which experiences additional ionisation and heating by each quasar to 5 proper Mpc, matching the size of the near-zones analysed in Bolton et al. (2011).

Chapter 3

Modelling of ionising sources

We next discuss the parametrisation of ionising sources in our model, encapsulated by the redshift-dependent parameter $N_{\rm ion}$, the number of ionising photons entering the IGM per baryon in galaxies. We begin by describing existing observational constraints on the IGM ionisation state and then proceed to discuss how these are used to calibrate $N_{\rm ion}$ and its evolution with redshift.

3.1 Observational constraints on $N_{\rm ion}$

3.1.1 The ionisation rate from the Lyα forest opacity

Firstly, observations of the Lyα forest in quasar absorption spectra can be used to infer the ionising background due to luminous sources. The measured quantity is the mean transmission of Lyα flux, $\langle F \rangle$, along the line of sight, or equivalently the effective optical depth $\tau_{\rm eff} = -\log \langle F \rangle$. This is related to the background photoionisation rate per hydrogen atom ($\Gamma_{\rm HI} = \Gamma_{-12} \times 10^{-12}\,{\rm s}^{-1}$) using a series of assumptions collectively referred to as the Fluctuating Gunn-Peterson Approximation (FGPA). The FGPA assumes that the IGM is in photo-ionization equilibrium, which is justified in the low density regions of the Lyman-α forest. Then, ignoring the effects that peculiar velocities and thermal broadening have on absorption, the optical depth at the Lyman-α frequency ν_{Ly_α} is:

$$\tau = \frac{\pi e^2 f_{Ly_\alpha}}{m_e \nu_{Ly_\alpha} H(z)} n_{\rm HI} \tag{3.1}$$

for an oscillator strength of f_{Ly_α}. However, in equilibrium, and assuming collisional ionization to be unimportant at low density, the neutral hydrogen density is just the balance of photo-ionizations and recombinations:

TABLE 3.1: Photo-ionisation rate constraints from the Lyα forest opacity obtained by Bolton et al. (2005) and Wyithe & Bolton (2010). The most likely value and errors at 68 per cent confidence intervals for the parameter $N_{\rm ion}$, which we subsequently derive, are also given.

Redshift	Γ_{-12}	$N_{\rm ion}$
4	$0.97\pm^{0.48}_{0.33}$	$35.3\pm^{17.5}_{12.1}$
5	$0.47\pm^{0.3}_{0.2}$	$22.7\pm^{14.3}_{9.7}$
6	$0.18\pm^{0.18}_{0.09}$	$13.0\pm^{13.0}_{6.5}$

$$n_{\rm HI} = \frac{\alpha_{\rm HII} n_{\rm HeII} n_{\rm e}}{\Gamma_{\rm HI}} \tag{3.2}$$

where $\alpha_{\rm HII}$ is the recombination rate as described in Section 2.5.

The effective optical depth is related to τ as its average over many lines of sight. Therefore, in order to infer $\Gamma_{\rm HI}$ from $\tau_{\rm eff}$, we must compare to the statistics of many lines of sight taken from hydrodynamical simulations. Comparisons to these simulations must make the further simplifying approximation that baryons trace dark matter and have a temperature defined by a simple power law relationship to density $T = T_0 \Delta^{\gamma-1}$ with $\Delta = (1+\delta)$. We note that this relation is only strictly true in thermal equilibrium and as will be discussed in Section 4, reionization has the effect of significantly flattening and broadening the relation's scatter. However, so long as a broad enough uncertainty on the power law index γ is taken into account, and translated to an uncertainty on $\Gamma_{\rm HI}$, this should not matter.

Under these circumstances, and additionally assuming that the recombination rate scales as $\alpha_{\rm HII} \propto T^{-0.7}$ with the density of electrons and He II being just the hydrogen density, the optical depth is

$$\tau = \tau_0 \frac{(1+z)^6 (\Omega_b h^2)^2}{T_0^{0.7} H(z) \Gamma_{\rm HI}} \Delta^{2-0.7(\gamma-1)} \tag{3.3}$$

where τ_0 is a constant encapsulating the recombination rate and the normalising fraction in equation 3.1. Using full hydrodynamical simulations and equation 3.3 we may relate $\tau_{\rm eff}$ to Γ_{-12}. This has been done by Bolton et al. (2005) and Wyithe & Bolton (2010) who have measured Γ_{-12} at $z = 4-6$ to have the values shown in Table 3.1.

These measurements may then be compared to our own simulated ionisation rate, which is calculated using equation (2.8). Combined with equations (2.3 - 2.7), evaluated for the case of a uniformly ionised IGM at $z < 6$ this then yields constraints on $N_{\rm ion}$, which are also shown in Table 3.1.

3.1.2 THOMSON OPTICAL DEPTH TO CMB PHOTONS

The electron scattering optical depth provides an integrated constraint on the IGM ionisation state throughout the epoch of reionisation. We use results from the latest WMAP observations, $\tau_{\rm CMB} = 0.088 \pm 0.015$ (Komatsu et al. 2011). This is related to the ionisation history by

$$\tau_{\rm CMB} = \int_0^{z_{\rm CMB}} c\frac{dt}{dz} Q(z)\,(1 + f_{\rm He}(z))\,n_{\rm H}(z)\sigma_{\rm T} dz, \tag{3.4}$$

where $\sigma_{\rm T}$ is the Thomson scattering cross-section, $n_{\rm H}$ is the hydrogen number density and $f_{\rm He}$ is a correction factor due to the presence of ionised helium. In our model, we assume that the ionisation of He I traces that of H I , whilst He II is instantaneously ionised at $z = 3$. The ionization history $Q(z)$ itself may be evaluated for any given parametrization of $N_{\rm ion}(z)$ using equation 2.2. We are therefore able to obtain a realization of $\tau_{\rm CMB}$ for any given $N_{\rm ion}(z)$.

3.2 Parametrisation of $N_{\rm ion}$

Using these observations, we may now constrain possible parametrisations of $N_{\rm ion}$ in our model. There is considerable theoretical uncertainty concerning the exact shape of $N_{\rm ion}$, particularly for $z > 6$, where there are no direct observations. This is primarily because $N_{\rm ion}$ encapsulates a number of physical effects, each of which is itself highly uncertain. To see this, we may decompose it into three key parameters; a fraction of baryons incorporated into stars $f_\star$, a number of ionizing photons emitted per baryon in stars $N_{\rm UV}$ and an escape fraction of photons from galaxies $f_{\rm esc}$:

$$N_{\rm ion} = N_{\rm UV} f_\star f_{\rm esc} \tag{3.5}$$

Of these parameters, probably the most uncertain is the star formation efficiency $f_\star$. This uncertainty derives from the various feedback mechanisms that determine whether baryons will fall into galaxies and subsequently form stars. It is clear that winds from exploding stars will alter the rate at which baryons collapse, but whether they act to initiate or quench star formation is not so clear. At the same time, the photo-heating caused by reionization will tend to drive baryons out of galaxies leading to a decrease in $f_\star$. However, it is hard to determine if this is a permanent or dominant effect. Therefore, the behaviour of $f_\star$ suggests an increase in $N_{\rm ion}$ to high redshift, but with no certainty.

Meanwhile, the escape fraction of ionising photons also has a high degree of uncertainty. This comes primarily from the presence of dust, large particles that absorb UV radiation and re-emit in the infrared, in galaxies. Since dust is drawn from the debris of exploded stars, the escape fraction is thought to increase towards high redshift

(Wyithe et al. 2010) where fewer supernovae occurred thereby decreasing the dust content. However, we should note that this interpretation of the redshift dependence of $f_{\rm esc}$ has a much weaker evolution at high redshifts during which the EoR is though to occur. Therefore, any modelling of $N_{\rm ion}$ must account for an upward evolution of $f_{\rm esc}$ with redshift, which remains relatively weak at high redshift.

Finally, the number of ionizing photons emitted once baryons collapse into stars is relatively well constrained. Given an initial mass function (IMF) of stars, which gives the fraction of stars in any mass range, and an average metallicity, which measures the abundance of heavier elements, we can theoretically calculate $N_{\rm UV}$ to high precision. In addition, the IMF can be measured and parametrised very well at the present day using the Salpeter formulation (Salpeter, 1955). Nevertheless uncertainty does arise from how exactly the IMF and metallicity evolve to high redshift, particularly at the start of the EoR. It is evident that the earliest stars will be metal-poor since metals are only produced by the fusion in stars and distributed by supernovae. Moreover, this reduced metallicity will tend to produce much heavier stars, leading to a net increase in $N_{\rm UV}$. However, how quickly the first generation of stars disappear and evolve to the present day observed stellar populations remains unclear.

What we may conclude from all these uncertainties is that $N_{\rm ion}$ probably increases with redshift, but with what dependence we do not know. Even when observational constraints are applied to our knowledge of $N_{\rm UV}$, $f_{\rm esc}$ and $f_\star$ it remains hard to determine the evolution of $N_{\rm ion}$. Indeed, several studies (Pritchard et al. 2009; Mitra et al. 2011) have found that it is effectively unconstrained in the range $6 < z < 11$. This is encapsulated in Figure 3.1 from Mitra et al. (2011), which shows the modelling errors on $N_{\rm ion}$ using constraints from the ionizing background and the electron scattering optical depth. We note that the ionizing efficiency is well characterised at low redshift by Γ_{-12} and at high redshift by $\tau_{\rm CMB}$. However, during the entire EoR, when the filling factor of neutral hydrogen is evolving from 0 to 1, $N_{\rm ion}(z)$ is essentially unknown. Therefore, in order to correctly capture this uncertainty, and to explore the sensitivity of our simulated temperatures to changes in the parametrisation, we choose to employ two different models for the redshift evolution of $N_{\rm ion}$.

3.2.1 LINEAR MODEL

The simplest model, and one often used in previous simulations of reionisation (e.g. Haiman & Loeb 1997; Geil & Wyithe 2008), assumes a single redshift independent parameter. However, this cannot be reconciled with measurements of the photo-ionisation rate from the Lyα forest at $z \leq 6$, so we employ a slight variant on the model. We take $N_{\rm ion}$ to be a constant up to the reionisation redshift, which is found by solving equation (2.2) for a universe that is fully ionised by the desired redshift. This effectively fixes the reionisation history for any given $z_{\rm r}$. Then, to ensure consistency with observations of Γ_{-12}, we allow $N_{\rm ion}(z)$ to evolve linearly once reionisation is complete in order

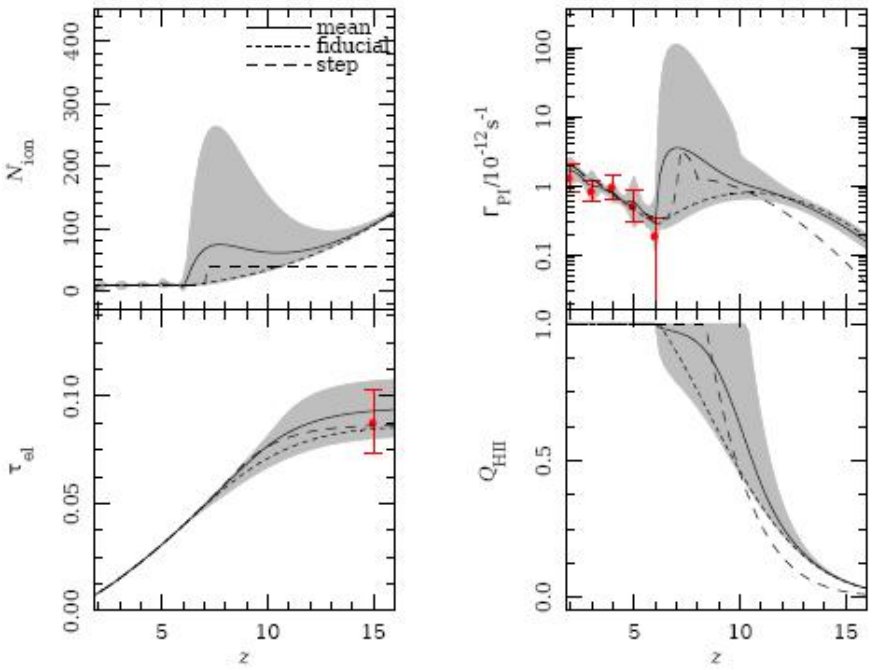

FIGURE 3.1: Evolution of the number of ionising photons per baryon which escape into the IGM, $N_{\rm ion}$ (top left), and the H II filling factor, Q (bottom right). In each case, we show the optimal evolution (black solid line) alongside the 95 % confidence limits (grey shaded regions). For comparison, we also show fits to the electron scattering optical depth (bottom left) and the IGM ionization rate (top right) with observed constraints shown in red. We note that the evolutions are well modelled at high and low redshift but remain highly uncertain during the EoR. Figure taken from Mitra et al. (2011).

to best fit the data points at $z < 6$. This is broadly consistent with predicted increases in the escape fraction and $N_{\rm UV}$ discussed in the previous section. For this model, we do not have the freedom to fit to the electron scattering optical depth. We will therefore defer discussion of the constraints it imposes on our model to Chapter 5.

3.2.2 CUBIC MODEL

We also explore arbitrary ionisation histories that best match the $\tau_{\rm CMB}$ constraint, by employing a model that is redshift-dependent prior to $z_{\rm r}$. To ensure enough freedom to match all constraints, we refer to Mitra et al. (2011), which used a principal component analysis to conclude that most of the uncertainty in $N_{\rm ion}(z)$ could be sufficiently described by 4 free parameters. We therefore choose to follow the approach of Pritchard et al. (2009) and model $N_{\rm ion}$ as a cubic function, allowing for a large variety of different evolutions:

$$N_{\rm ion}(z) = (N_{\rm p} - N_0)\left[4\left(\frac{z-z_0}{\Delta z}\right)^3 - 3\left(\frac{z-z_0}{\Delta z}\right)\right] + N_0, \tag{3.6}$$

where we have parametrised by the midpoint (z_0, N_0), and the peak $\left(z_0 + \frac{\Delta z}{2}, N_{\rm p}\right)$. For each reionisation redshift, we fit this curve to the measured electron scattering optical depth and the ionisation rate at $z = 4 - 6$. As in Pritchard et al. (2009), we impose a prior on the comoving emissivity of $\dot{N}_\gamma < 10^{51}{\rm s}^{-1}{\rm Mpc}^{-3}$ to disallow unphysically large ionising backgrounds. We stress that this model is not physically motivated and clearly overfits the limited data we use. But as we do not seek to exactly find $N_{\rm ion}$ but only to view the effect of different ionisation histories on simulated IGM temperatures, this does not significantly impact upon our results.

The optimal evolutions of $N_{\rm ion}$ and the filling factor Q for the cubic and linear models are shown in Figure 3.2 for $z_{\rm r} = 6.5$ and $z_{\rm r} = 9.0$. For both cases, the behaviour of the emissivity matches quite well to evolutions derived elsewhere (Choudhury & Ferrara 2006; Pritchard et al. 2009; Mitra et al. 2011), and fulfils our expectation of a general downward evolution of $N_{\rm ion}(z)$. However, for early reionisation in the cubic model, star formation switches on later and the filling factor develops more quickly than is probably physical in order to match the electron scattering constraint. This is not necessarily undesirable as the aim in modelling $N_{\rm ion}$ is not to produce the most physically plausible model, but to explore the full range of possible evolutions. In this respect we succeed as the two models do provide very different ionisation histories at each $z_{\rm r}$. Therefore they should allow us to probe the sensitivity of our temperature predictions to realistic variations in the ionising background.

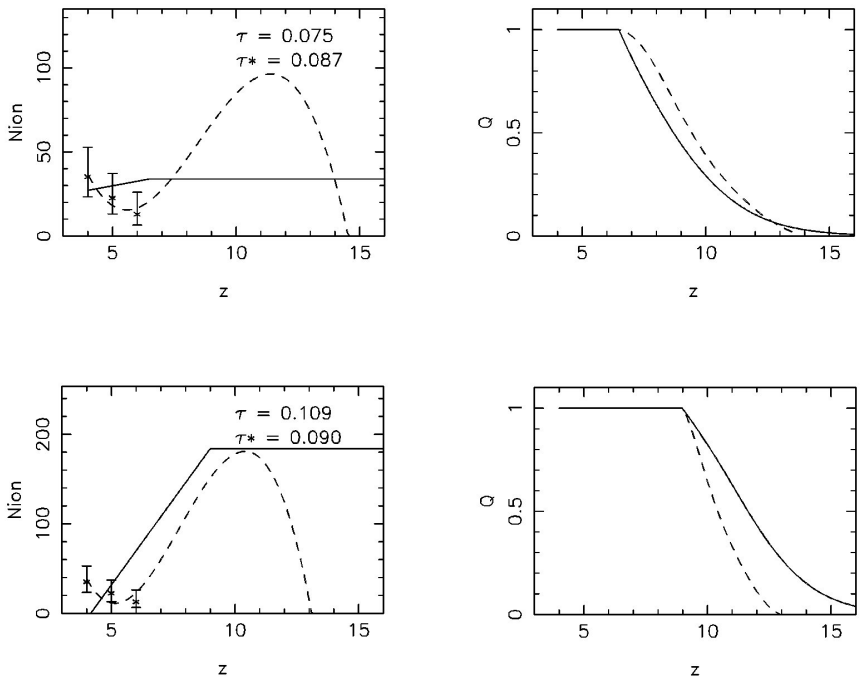

FIGURE 3.2: Evolution of the number of ionising photons per baryon which escape into the IGM, $N_{\rm ion}$ (left hand columns), and the H II filling factor, Q (right hand columns) for reionisation histories with $z_{\rm r} = 6.5$ (top) and $z_{\rm r} = 9.0$ (bottom). Solid curves show the evolution for the linear $N_{\rm ion}$ model, whilst the case of the cubic $N_{\rm ion}$ is shown by the dashed lines. The plotted points represent constraints imposed by values of Γ_{-12} obtained from the Lyα forest opacity by Bolton et al. (2005) and Wyithe & Bolton (2010). The inset in the left hand panels gives the electron scattering optical depth for the constant and cubic $N_{\rm ion}$ models (τ and $\tau*$, respectively).

Chapter 4

Results

4.1 The IGM thermal state following reionisation

Using the semi-numerical model described in the previous two sections, we may now examine the variation of IGM temperature with reionisation redshift. For any given $z_{\rm r}$, and for each of the two different parametrisations of $N_{\rm ion}$, we compute an optimal evolution that ensures $Q = 1.0$ by $z_{\rm r}$. Using the calculated ionising background, we then calculate the temperature field over the redshift range $5.5 < z < 6.5$, around the time when the observed quasars switch on.

4.2 The Redshift of Reionization

In Figure 4.1 we show slices through our simulation box for a model where reionization is complete by $z_{\rm r} = 6.0$ and the ionizing efficiency is set by the linear model for $N_{\rm ion}$. In general, we capture the same topology of inhomogeneous reionization simulated using the full hydrodynamical code of Trac et al. (2008) as shown in Figure 4.2. Specifically, the reionization redshift at individual voxels correlates strongly with the large scale density field reflecting the bias of ionizing sources towards high density regions, which collapse first. In addition, we accurately model the timescale of reionization, which initially proceeds slowly around small spherical sources but finishes very rapidly as the low density IGM, comprising over 50 $\%$ of the field, is ionized in $\Delta z \sim 0.5$.

The temperature field at the end of reionization similarly reflects the features of the full hydrodynamical model. Firstly, the highest temperatures are registered at the cores of the regions that were ionized first and correspondingly have a high enough density to continually photo-heat the gas. We lack the resolution to accurately model the filamentary nature of these regions, or to calculate the high temperatures which result from shock heating. However, as they represent a statistically small population

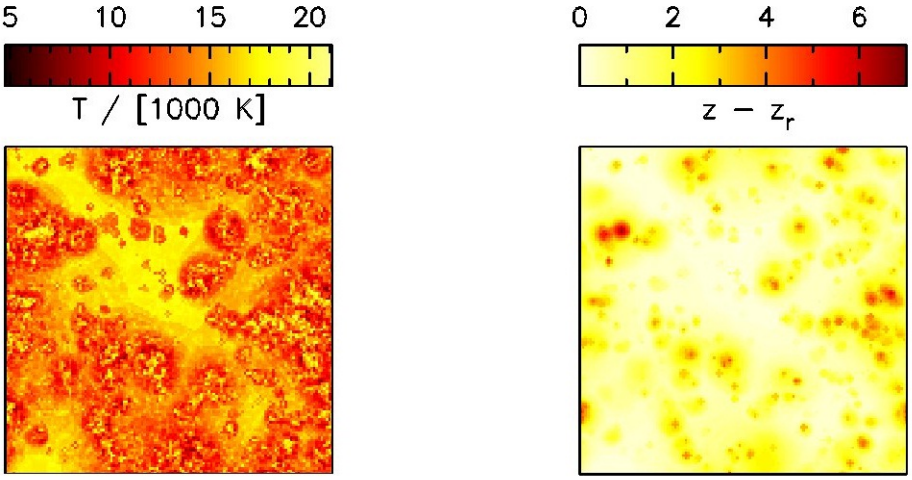

FIGURE 4.1: Maps of a 2D slice through the centre of our simulation box at $z = 6.0$ prior to the inclusion of any quasar heating for $z_{\rm r} = 6.0$ and the linear $N_{\rm ion}$ model. *Left:* Map of ionisation redshift for individual voxels. *Right:* Temperature at the measurement redshift ($z = 6.0$).

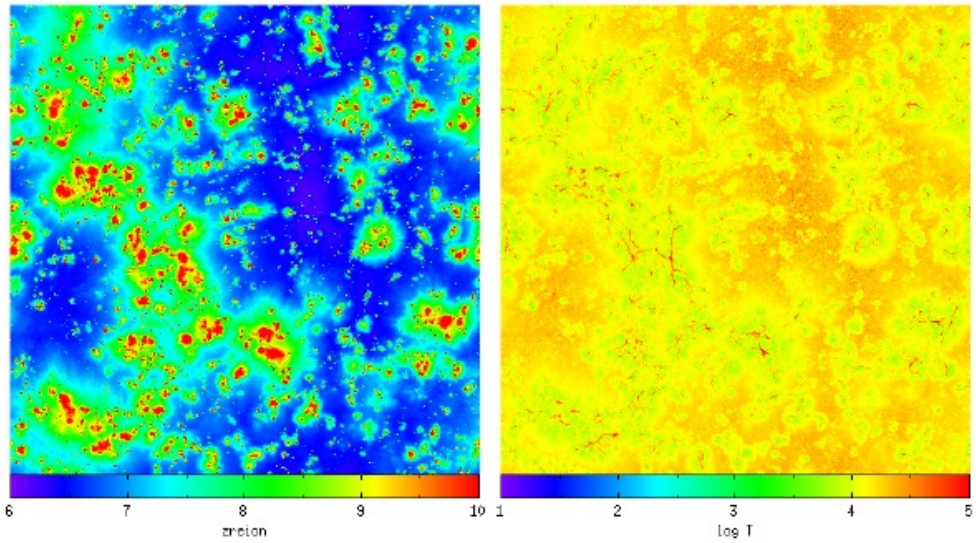

FIGURE 4.2: Maps of a 2D slice through the centre of the hydrodynamical simulation from Trac et al. (2008) for $z_{\rm r} = 6.0$. *Left:* Map of ionisation redshift for individual voxels. *Right:* Temperature at the measurement redshift ($z = 6.0$).

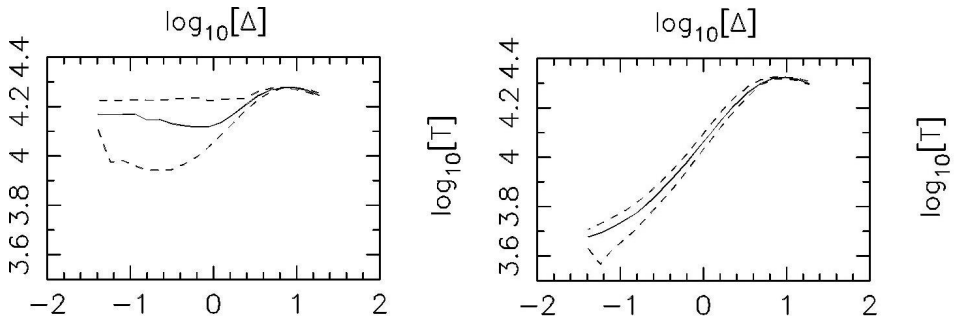

FIGURE 4.3: Gas temperature-density relations at redshift $z = 6$ for our semi-numerical model of reionization with $z_{\rm r} = 9.0$ (right) and $z_{\rm r} = 6.0$ (left). The late reionization model has an inverted power-law relation for the low-density IGM, with slope $\gamma - 1 \sim -0.2$ and order unity scatter. Meanwhile the early reionization model has settled into a rising power law with only small scatter.

of points, whose density is anyway not modelled accurately (see Section 2.5), this is unimportant for the calculation of temperature in the IGM.

On the other hand, in the more prevalent low density regions, we are able to model the temperature accurately. In particular, we note that the coolest gas immediately surrounds the highest density regions, as these were ionized early and so had longer to cool. Moreover, the low-density gas gets progressively warmer as we move away from sources and toward the voids. It is apparent from the maps that we are capturing the inverse relationship between the reionization redshift and temperature, which is present in the hydrodynamical simulations.

4.2.1 THE TEMPERATURE-DENSITY RELATION

Figure 4.3 shows the gas temperature-density relations at $z = 6.0$ for two different reionization models, with $z_{\rm r} = 6.0$ and $z_{\rm r} = 9.0$ respectively. For each density bin of width 0.1 dex, we plot the median temperature and the 68 $\%$ confidence limits around it. For comparison, we also show analagous results from Trac et al. (2008) in Figure 4.4 displaying the temperature-density relation at the end of reionization and at $z = 4$ for a reionization model with $z_{\rm r} = 9.0$.

For the early reionization model, $z_{\rm r} = 9.0$ (right), the relation, in the hydrodynamical model, shows a tightly constrained power law dependence with $\gamma - 1 \approx 0.5$ for $T = T_0 \Delta^{\gamma - 1}$. This is characteristic of an IGM with no thermal memory of reionisation, where the temperature has reached an equilibrium between photoheating and recombination that only depends on the density. As before, our model fails to reproduce this at the very high-density end of the temperature-density relation as we do not account for shock heating. However, outside of this region, we do capture the correct power law

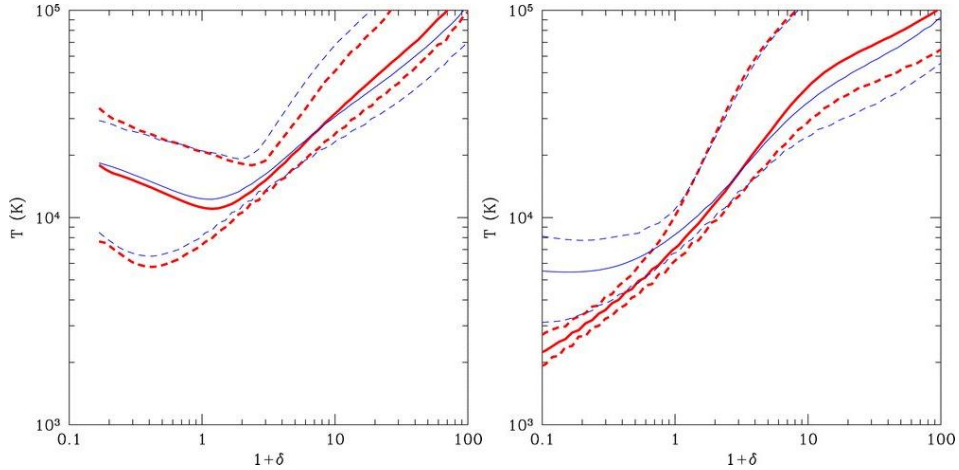

FIGURE 4.4: Gas temperature-density relations at the end of reionization (left) and at a redshift $z = 4$ (right) for the hydrodynamical reionization models of Trac et al. (2008). We show results for both $z_{\rm r} = 9.0$ (red thick lines) and $z_{\rm r} = 6.0$ (blue thin lines), but focus on the $z_{\rm r} = 9.0$ model, which correctly captures the difference in measured temperature-density relation at $z = 6$ between early and late reionization models. For each density bin of width 0.05 dex, we show the median temperature (solid lines) and the 2-σ spread (dashed lines).

slope and relatively small scatter.

More importantly, in the case of late reionisation, we are able to correctly model the inversion of the temperature-density relation at low densities. The left panel of Figure 4.3 shows much wider 68% confidence limits (dashed lines) below the highest densities, with an inverted power-law slope of $\gamma-1 \approx -0.2$ for low densities ($\Delta < 1.0$). This anti-correlation between temperature and density arises due to the fact that lower density regions tend to be ionised last allowing them less time to cool. Similarly, the increased scatter comes about since some low density regions, which surround the first H II bubbles, will be ionized early and cool for longer. The scatter is therefore just a reflection of the spread in ionization times. This agrees well with Figure 4.4 and results from other previous studies (Bolton et al. 2004; Trac et al. 2008; Furlanetto & Oh 2009).

4.2.2 DIFFERENT REIONIZATION SCENARIOS

We now turn to comparisons of different reionization models within our semi-numerical code. In the top left-hand panels of Figure 4.5 we present temperature maps, at $z = 6.0$ calculated using our constant $N_{\rm ion}$ model, for reionisation completing by $z_{\rm r} = 6.5$ and $z_{\rm r} = 9.0$. For comparison, maps of the voxel ionisation redshifts relative to the redshift at which reionisation completes, $\Delta z = z - z_{\rm r}$, are also shown in the corresponding central panels. We note that the structure of ionised bubbles at fixed Δz is very similar for the early and late models. In the case of late reionisation, the temperature mimics

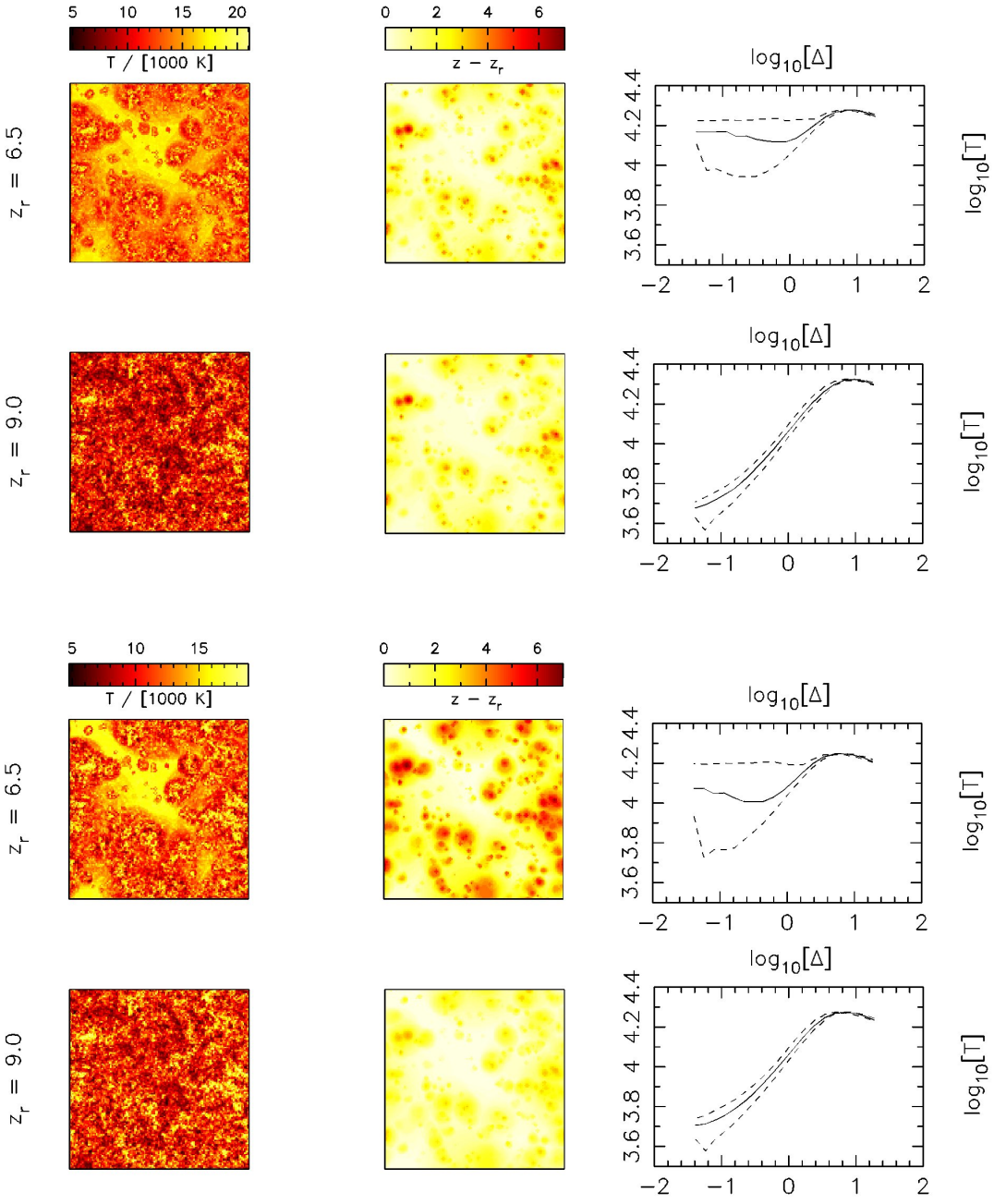

FIGURE 4.5: Maps of a 2D slice through the centre of our simulation box at $z = 6.0$ prior to the inclusion of any quasar heating. The upper six panels show results for the linear $N_{\rm ion}$ model while the lower set show the same results allowing for a cubic $N_{\rm ion}$. In each set the top row indicates maps for reionisation occurring at $z_{\rm r} = 6.5$ and the lower row for $z_{\rm r} = 9.0$. *Left Hand Panels:* Temperature at the measurement redshift ($z = 6.0$). *Central Panels:* Map of ionisation redshift for individual pixels. *Right Hand Panels:* Temperature (T) against density contrast (Δ) at $z = 6.0$, displaying both the median (solid) and 68% confidence intervals around the median (dashed).

this ionisation structure, with cooler regions centred on the small H II bubbles that were ionised first, and have thus had more time to cool. However, regions of the IGM ionised during the overlap phase retain a clear imprint of heating. The situation is very different for early reionisation, where the temperature field shows little correlation with the ionisation topology. Instead, the temperature largely reflects the random Gaussian structure of the density field, indicating that even with reionisation occurring as late as $z_{\rm r} = 9.0$, the temperature has already predominantly settled to an asymptotic state by $z = 6.0$.

The same set of results can also be seen for the cubic model of $N_{\rm ion}$ in the lower set of panels. In this case, the growth of ionised bubbles is significantly different at constant $\Delta z = z - z_{\rm r}$ for the separate reionisation redshifts. As described in Section 3.2, late reionisation ($z_{\rm r} = 6.5$) is a more gradual process in this model, with ionisation times spread more evenly around the H II bubbles. This has the effect of spreading out the IGM temperatures, so that regions ionised early tend to be cooler. Similarly, the scatter in the temperature-density relation is increased. On the other hand, for $z_{\rm r} = 9.0$, reionisation is far more rapid, effectively occurring over a redshift interval of $\Delta z = 3.0$. Despite this difference, the temperature field evolves, by $z = 6.0$, to the same asymptotic state as for the constant model (with a slightly reduced scatter in the temperature-density relation due to the more abbreviated differences in ionisation time). This reaffirms the conclusion that the thermal memory of reionisation for $z_{\rm r} = 9.0$ is almost completely absent by $z = 6.0$.

To see this more clearly, we consider how the mean and standard deviation of the overall temperature distribution at $z = 6.0$ evolve as a function of reionisation redshift (in Figure 4.6). We note that for both models the mean temperature only varies by several hundred Kelvin above $z_{\rm r} \approx 9.0$, although an asymptotic state is probably only fully reached for $z_{\rm r} \approx 10.5 - 11.0$. For later reionisation, the temperature distributions vary quite rapidly, and at $z_{\rm r} = 6.0$ the IGM is heated to 5000 K above its thermal asymptote in the constant $N_{\rm ion}$ model. This result is slightly more muted for the cubic model, as the elongated reionisation history means that large regions of the IGM have longer to cool, thereby reducing the thermal imprint. However, even allowing for this, unit changes in the reionisation redshift lead to temperature variations of up to 1500 K by $z = 6.0$. As this is comparable to the standard deviation of the distributions it means that changes of $\Delta z_{\rm r} \approx 1.0$ should be distinguishable on the basis of temperature measurements for $z_{\rm r} < 9.0$, but will require very precise data.

4.3 Temperature in a Quasar Proximity Zone

We next consider how our predicted temperatures compare with observations drawn from (Bolton et al., 2011). In their study, the width of absorption lines in Lyα forest spectra were used to calculate the temperature at mean density around 7 quasars in the range $5.5 < z < 6.5$. By comparing to synthetic spectra generated from a suite of

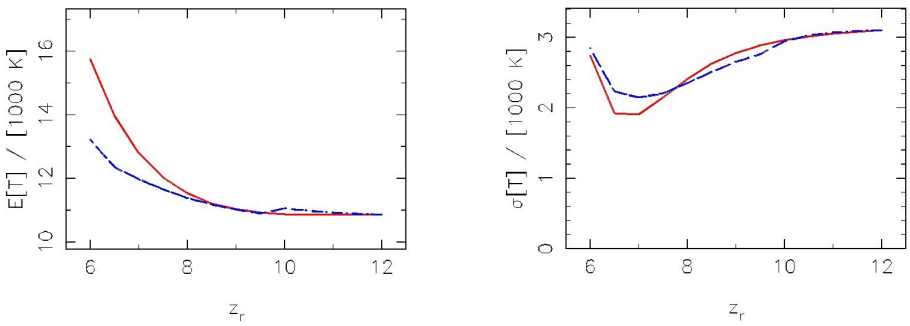

FIGURE 4.6: Mean (Left panel) and standard deviation (Right panel) of the simulated temperature distributions at $z = 6.0$ prior to the inclusion of quasar heating. In both cases we show results for two different models; the constant $N_{\rm ion}$ model (solid lines) and the cubic model allowing for an evolving $N_{\rm ion}$ (dashed lines).

hydro-dynamical simulations at different temperatures, they find temperatures at mean density (T_0), averaged over the proximity zone ($2.6 \leq R \leq 33$ Mpc) for the different quasar observations.

In Figure 4.7 we show their measurements of T_0 for each of the individual quasars. The points in red indicate results obtained using the fiducial calibration simulations in Bolton et al. (2010). Meanwhile those in blue represent the results they obtained after allowing for the possibility of an increased Jeans presure smoothing scale, as might be expected if IGM heating from reionization extends to much higher redshifts than assumed in the fiducial simulations, with $z_{\rm r} \sim 12 - 15$. While the fiducial model is probably preferred as the reionization redshift is unlikely to be so large, we still compare to both sets of observations and take the different results to bracket the range of possible constraints.

4.3.1 COMPARISONS

In order to compare these observations to our model, we calculate the distribution of model temperatures for each quasar. At any given voxel, we switch on a quasar at $t_{\rm q} = 1.5 \times 10^7$ years prior to the redshift at which the quasar was measured, and use the procedure outlined in Section 2.6 to calculate the surrounding IGM temperature. We then construct 200 random sightlines through the proximity region and for each one derive a temperature-density relation for all voxels. This relation may be used to infer a temperature at mean density for every sightline. Repeating this procedure for quasars centred on all voxels in the simulation box gives a distribution over possible sightline temperatures for a single observed quasar.

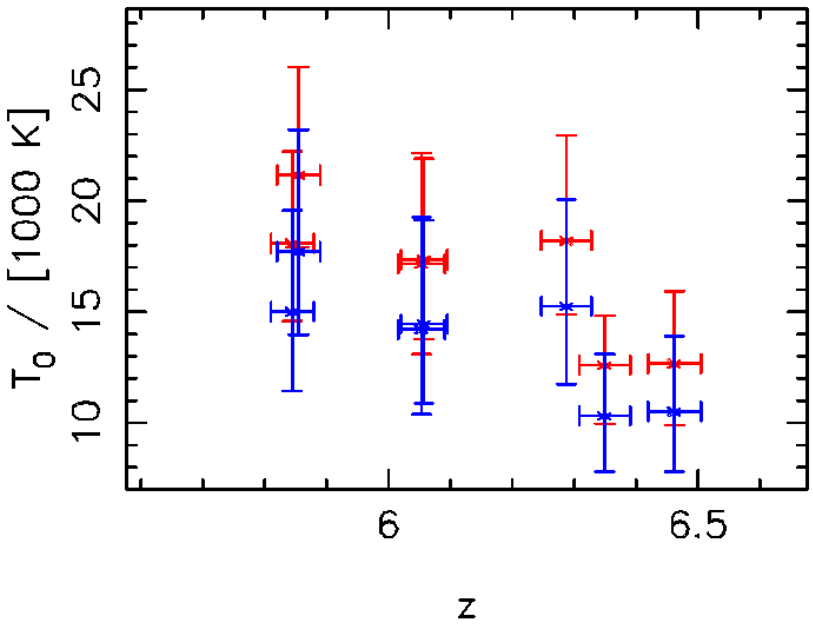

FIGURE 4.7: Constraints on the temperature of the IGM as a function of redshift in the proximity zone of 7 quasars. We show two families of points; The results in red come from the fiducial model of Bolton et al. (2010), while those in blue are the same except for a larger assumed Jeans smoothing scale. Error bars in temperature indicate the 68 per cent confidence intervals around the median, and error bars in redshift represent the range covered by each quasar proximity zone.

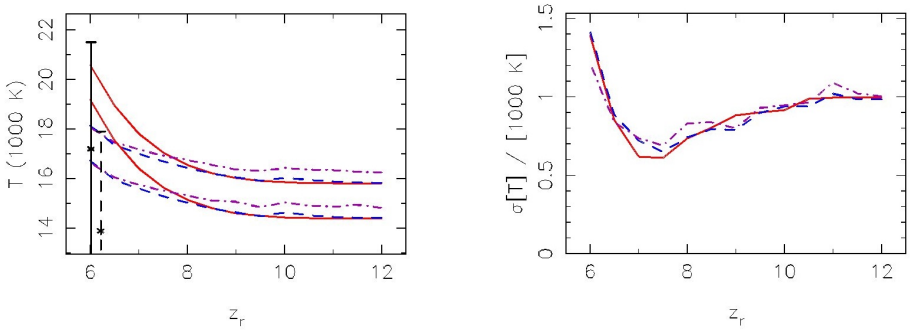

FIGURE 4.8: Mean and standard deviation of the simulated distributions over temperature at mean density ($p(T_0|z_\mathrm{r})$) in a quasar proximity zone at $z = 6.02$. *Left:* Simulated mean for three different cases, the constant N_ion model (solid lines), the cubic model (dashed lines), and the cubic model accounting for the density bias of quasars (dot-dashed lines). We show simulated temperatures for $\alpha_\mathrm{q} = 2.0$, which yield the low temperature distributions and $\alpha_\mathrm{q} = 1.0$ giving higher temperatures. For comparison, we also show the measured temperature and 68% confidence limits for a quasar observed at the same redshift. We display both the fiducial measurement (solid black) and the measurement found by assuming a larger Jeans smoothing scale (dashed black). *Right:* Standard deviations for the aforementioned models. In this case we only show results for $\alpha_\mathrm{q} = 1.0$, however standard deviations are similar regardless of quasar spectral index.

In Figure 4.8 we show the mean and standard deviation of the simulated distributions for a quasar observed at $z = 6.02$, corresponding to one of the observations from (Bolton et al., 2011). Results are displayed for both hard ($\alpha_{\rm q} = 1.0$) and soft ($\alpha_{\rm q} = 2.0$) quasar spectra. These retain all the features of the temperature distributions prior to quasar heating, including the flattening of the mean by $z_{\rm r} \approx 9.0$, and the reduction of scatter above $z_{\rm r} = 8.0$. The standard deviations tend to be slightly smaller, particularly at large $z_{\rm r}$, due to the fact that we are only considering temperature at mean density. This then allows for even sharper distinctions between reionisation redshifts.

We find that the difference in measured temperature between early and late reionisation is only $2\,500$K, corresponding to around 2-σ difference in the simulated distributions. Given that uncertainties in the measurement of individual temperatures are around $\pm 3\,000$K, it is unlikely that a strong constraint can be obtained from any single observation. However, the combination of all 7 observations effectively reduces the measurement error to $\pm 1\,200$K, which combined with the simulated scatter gives a 1-σ uncertainty of $\pm 1\,500$K. Therefore, the observations will be able, in principle, to distinguish between early and late reionisation scenarios.

The unknown quasar spectral index introduces additional uncertainties into the interpretation of temperature. For example, in the cubic model, the temperatures obtained for late reionisation and soft quasar spectra are almost identical to those obtained for early reionisation and a much harder spectra. Unfortunately, there are relatively few observations that constrain high-redshift quasar spectral index, with a recent study showing that the range $1.0 \leq \alpha_{\rm q} \leq 2.0$ is quite plausible (Wyithe & Bolton 2010). Thus, better constraints on $\alpha_{\rm q}$ may be required in order to make meaningful predictions on reionisation redshift. This is particularly true for the fiducial measurement, which encompasses the whole range of possible scenarios. In the model which assumes a larger Jeans scale however, the measurements are sytematically lower and only really fit the scenario of early reionization and soft quasar spectra. For this case, we may be able to rule out late reionization with some confidence.

Further modelling may also be required to account for uncertainties in quasar evolution. We have considered a single quasar episode prior to observation. However more complex duty cycles, which allow for helium recombination between quasar heating episodes could add significantly to the temperatures discussed here. On the other hand, shorter quasar lifetimes, which do not fully heat the IGM out to $R = 33$ Mpc, could result in cooler proximity zone temperatures.

4.3.2 QUASAR DENSITY BIAS

When calculating the measured temperature distribution through the quasar proximity zone, we have thus far assumed a random distribution of quasar positions. However, quasars and their host galaxies tend to trace high density regions owing to the clustering bias of massive haloes. Before calculating the constraints on $z_{\rm r}$, we therefore model the

quasar density bias. We weight the temperature distribution calculated in 4.3.1 by the likelihood $\mathcal{L}_{\rm g}(\delta)$ of observing a quasar at that location

$$p(T|w) = \sum_{allvoxels} \delta(T(x) - T)\mathcal{L}_{\rm g}(\delta(x)). \tag{4.1}$$

The likelihood of observing a galaxy, and a corresponding resident quasar, is then estimated from the Sheth-Tormen (2002) mass function as

$$\mathcal{L}_{\rm g}(\delta) = \frac{(1+\delta)\nu(1+\nu^{-2p})e^{-a\nu^2/2}}{\bar{\nu}(1+\bar{\nu}^{-2p})e^{-a\bar{\nu}^2/2}}, \tag{4.2}$$

where $\nu = (\delta_{\rm c} - \delta)/[\sigma(M)]$, $\bar{\nu} = \delta_{\rm c}/[\sigma(M)]$, and $a = 0.707$, $p = 0.3$ are constants.

The results including this density bias are shown by the dot-dashed curves in Figure 4.8. There is a slight flattening of the temperature differences between different reionisation redshifts. This is due to the relatively early ionisation time of the high density regions where quasars are found, which allows them more time to cool to their asymptotic state. At large values of $z_{\rm r}$ the temperature is systematically increased by a small amount, as high-density areas are asymptotically hotter. The increased mean for early reionisation reduces the certainty with which the measurement of T_0 can differentiate between reionisation redshifts. However, this is a minimal effect which should not strongly affect our constraints on $z_{\rm r}$.

Chapter 5

Constraints on Reionisation History

In the remainder of the thesis, we calculate the constraints that recent and upcoming temperature measurements impose on the reionisation redshift. Aside from a number of hypothesised parameters including $C, M_{\rm min}, M_{\rm ion}$ and α, and hypothesised models for $N_{\rm ion}$, there are two critical free parameters, $z_{\rm r}$ and $\alpha_{\rm q}$, in the model of Section 2. For any combination of these, we may compute mock observations, which consist of possible sightline temperatures for each $z_{\rm r}$, $\alpha_{\rm q}$ and the $i^{\rm th}$ quasar measurement $q^{\rm i}(z_{\rm r}, \alpha_{\rm q}^{\rm i})$. It is then possible, using Bayes' Theorem, to infer the likelihood that any set of 7 independent sightlines $\{q^{\rm i}\}_{i=1}^{7}$ correspond to the 7 measured temperatures from (Bolton et al., 2010)

$$p(\{q^{\rm i}\}_{i=1}^{7}|\mathbf{D}, M) = \frac{p(\mathbf{D}|\{q^{\rm i}\}_{i=1}^{7}, M)p(\{q^{\rm i}\}_{i=1}^{7}|M)}{p(\mathbf{D}|M)}, \tag{5.1}$$

where $\mathbf{D}$ is the combination of observational constraints obtained from $\tau_{\rm CMB}$ and the quasar temperature measurements, M is one of our models for reionization, and $p(\mathbf{D}|M)$ is just a normalisation constant. The likelihood $p(\mathbf{D}|\{q^{\rm i}\}_{i=1}^{7}, M)$ can be easily found from the measured temperature distributions in Figure 4.7 and the measured errors on $\tau_{\rm CMB}$, which are taken to be Gaussian. Meanwhile the prior probability of choosing any set of sightlines $p(\{q^{\rm i}\}_{i=1}^{7}|M)$ is calculated from the density bias likelihood in equation 4.2 and the assumption that prior information on our free parameters is uniform over the ranges of interest, $1.0 \leq \alpha_{\rm q} \leq 2.0$ and $6.0 \leq z_{\rm r} \leq 12.0$. Redshifts outside this range are not considered as they are effectively ruled out at the lower end by Lyα flux data and at the upper end by the measurement of $\tau_{\rm CMB}$.

Using equation 5.1, we may find absolute bounds on the ionisation history by summing over sets of possible sightlines

$$p(z_{\rm r}|\mathbf{D}, M) = \sum_{\{q^{\rm i}\}} p(\{q^{\rm i}\}_{i=1}^{7}|\mathbf{D}, M)\delta[z_{\rm r}(\{q^{\rm i}\}_{i=1}^{7}|M) - z_{\rm r}] \tag{5.2}$$

since all sightlines in a given set are drawn from a single simulation box so they produce a definite prediction for $z_{\rm r}$. We note that the same does not hold true for the quasar spectral indices as each of the individual quasars may have different intrinsic spectra. Therefore, we only obtain constraints on each of the individual quasar spectra

$$p(\alpha_{\rm q}^{\rm i}|\mathbf{D}, M) = \sum_{\{q^{\rm i}\}} p(\{q^{\rm i}\}_{i=1}^{7}|\mathbf{D}, M)\delta[\alpha_{\rm q}^{\rm i}(\{q^{\rm i}\}_{i=1}^{7}|M) - \alpha_{\rm q}^{\rm i}] \tag{5.3}$$

Equations 5.2 and 5.3 produce model dependent estimates of our parameters of interest. This presents a problem as we are relatively uncertain of several aspects of our modeling, namely the ionizing efficiency $N_{\rm ion}$, the Jeans smoothing scale used to infer quasar temperatures in Bolton et al. (2011) and the biasing of quasars to high-density regions. Furthermore, from Figure 4.8 these modeling uncertainties can lead to significant variations in sightline temperature, particularly for late reionization.

Therefore, we would like to both compare the relative probability of our different models, and also obtain a less model dependent estimate of $z_{\rm r}$ and $\alpha_{\rm q}^{\rm i}$. We achieve this using Bayesian model comparison to calculate a posterior probability for model $M_{\rm i}$ given the data $p(M_{\rm i}|\mathbf{D})$

$$p(M_{\rm i}|\mathbf{D}) = \frac{p(\mathbf{D}|M_{\rm i})p(M_{\rm i})}{p(\mathbf{D})}, \tag{5.4}$$

where $p(\mathbf{D})$ is again just a normalisation constant and we assume a priori that all models are equally likely so that $p(M_{\rm i})$ is uniform. Model averaging can then be used to infer probabilities of free parameters across all models

$$p(z_{\rm r}|\mathbf{D}) = \sum_{i} p(z_{\rm r}|\mathbf{D}, M_{\rm i})p(M_{\rm i}|\mathbf{D}) \tag{5.5}$$

which provides a more general set of constraints on $z_{\rm r}$ and $\alpha_{\rm q}^{\rm i}$. They will still not be model independent as the set of models we consider are not complete. However, since our models bracket most of the physical uncertainties, they should be believable.

5.1 Constraints from the measured temperatures

In the upper panels of Figure 5.1, we present the resulting probability distribution functions over the parameter $z_{\rm r}$ for the linear $N_{\rm ion}$ model. The distributions are computed for the two different sets of measurements presented by Bolton et al. 2011, derived from their fiducial model (red solid curves) and a model with additional pressure (Jeans) smoothing in the IGM (blue dashed curves). The latter effectively lowers the near-zone temperature constraints by $\sim 3000\,{\rm K}$. The results are also shown both with (left panel) and without (centre panel) accounting for quasar density bias. Including the effect of

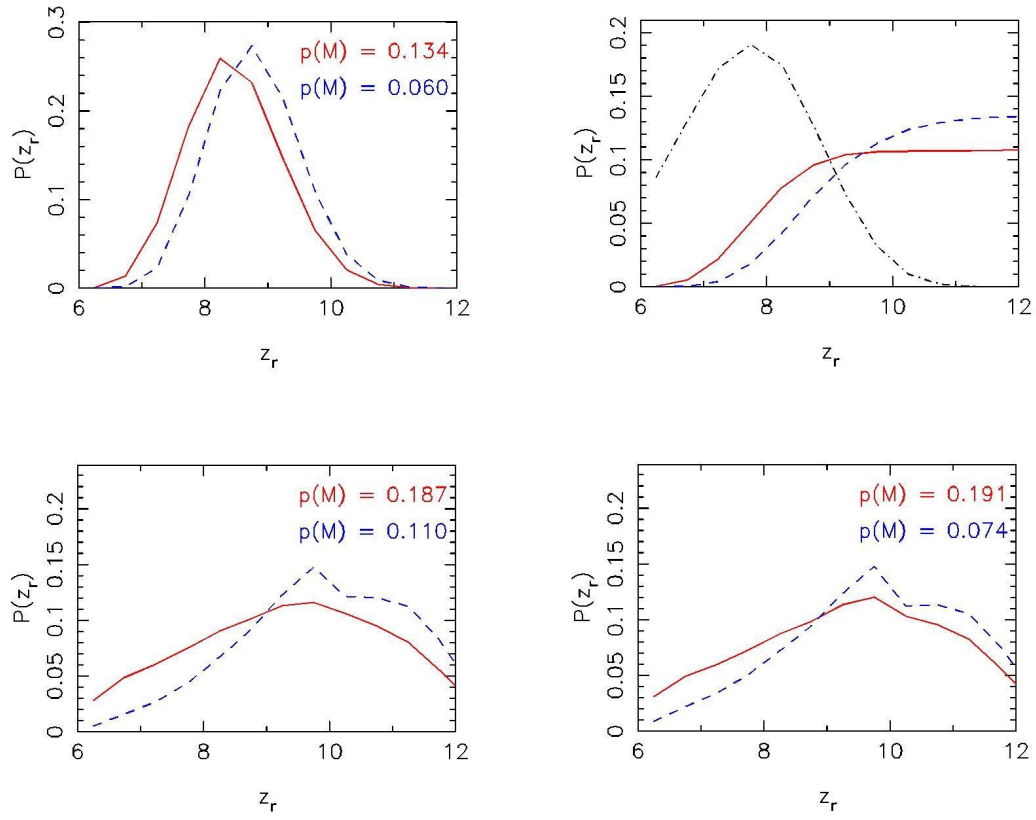

FIGURE 5.1: Constraints on reionisation redshift based on measured values of T_0, $\tau_{\rm CMB}$ and Γ_{-12} for different models of reionisation. In each case two probability distributions are shown, representing constraints from the fiducial near-zone temperature measurments of Bolton et al. (2010) (red solid curves) and allowing for a larger Jeans scale (blue dashed curves). The relative probabilities of each model are shown in the top corner of each plot. *Upper Left:* Constraints from T_0 and $\tau_{\rm CMB}$ and the linear model for $N_{\rm ion}$. *Upper Middle:* The same model, *Upper Right:* Constraints obtained from the near-zone temperatures and $N_{\rm ion}$ alone. For comparison, the constraint from $\tau_{\rm CMB}$ and $N_{\rm ion}$ is shown in black dot-dashed. *Lower Left:* The probability distributions for the cubic $N_{\rm ion}$ model. *Lower Right:* Distributions for the cubic model but now accounting for the bias of quasars to regions of high density.

TABLE 5.1: Bayesian model probabilities as well as 1 and 2-σ constraints on the reionization redshift for different reionization models. We show results for linear and cubic models of $N_{\rm ion}$, including or excluding density bias and both fiducial and Jeans smoothed observations.

$N_{\rm ion}$	Density Bias	Observations	p(M)	1-σ	2-σ
Linear	Yes	Fiducial	0.137	(7.403, 9.048)	(6.860, 9.971)
Linear	Yes	Jeans	0.047	(7.638, 9.379)	(7.125, 10.204)
Linear	No	Fiducial	0.137	(7.506, 9.045)	(6.879, 9.818)
Linear	No	Jeans	0.047	(7.997, 9.420)	(7.387, 10.153)
Cubic	Yes	Fiducial	0.201	(8.149, 10.935)	(7.003, 11.857)
Cubic	Yes	Jeans	0.103	(8.788, 11.182)	(7.635, 11.980)
Cubic	No	Fiducial	0.214	(8.157, 10.945)	(7.202, 11.904)
Cubic	No	Jeans	0.057	(8.912, 11.182)	(7.918, 11.974)

quasar density bias has very little effect on these results. For comparison, we also plot the individual distributions obtained by alternately considering constraints from either $\tau_{\rm CMB}$ and T_0 alone combined with our assumed $N_{\rm ion}$ evolution (right panel). As expected, the measurement of T_0 alone does not differentiate between early reionisation redshifts, as for all scenarios the IGM has reached an asymptotic temperature. However, the temperature data do provide constraining power for low $z_{\rm r}$. We find that irrespective of which set of temperature measurements from Bolton et al. (2011) is considered, very late reionisation is ruled out to high confidence. This is because the $5\,000{\rm K}$ increase in IGM temperature for $z_{\rm r} < 7.5$, pushes the mean quasar temperature well above the observations.

In the bottom panels of Figure 5.1 we show corresponding constraints for the cubic model. In this model the observed value of $\tau_{\rm CMB}$ is used in defining the parameters governing $N_{\rm ion}$. It is therefore a much weaker a-posteriori constraint and we can no longer rule out large reionisation redshifts. Similarly for low $z_{\rm r}$, the smaller temperature differences between reionization scenarios means that late reionisation cannot be excluded with the same confidence. Furthermore, the relatively tight constraints obtained when considering the temperatures derived assuming a larger Jeans scale are probably not to be believed. This can be seen if we consider the relative model probabilities in Table 5.1. We note that constraints from the fiducial measurements are favoured by a factor of around 3 over the larger Jeans scale measurements, making it unlikely that they are correct. On the other hand, the observations do not differentiate well between other modelling uncertainties, and the relative model probabilities for the models of $N_{\rm ion}$ and density bias are close to indistinguishable.

This is reflected in the final model averaged distribution of Figure 5.2 , which roughly corresponds to a mix of the fiducial results from the linear and cubic mod-

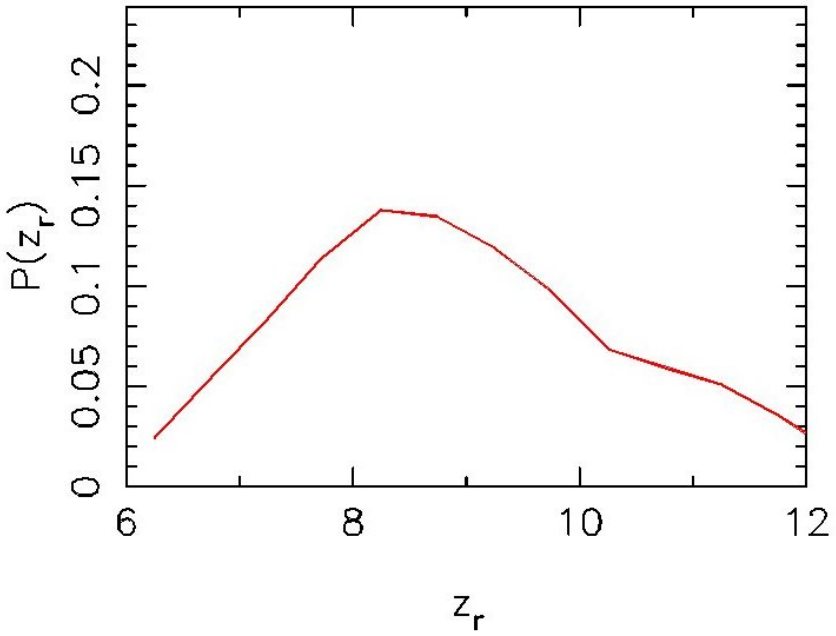

FIGURE 5.2: Constraints on reionisation redshift based on measured values of T_0, $\tau_{\rm CMB}$ and Γ_{-12} when averaged over all our different models of reionisation. This includes different models for $N_{\rm ion}$, the bias of quasars to high density regions and the Jeans pressure smoothing scale. Model averaging significantly weakens constraints as it adds uncertainties to the temperature, but still rules out late reionization to $z_{\rm r} > 7.9$ (6.5) at 68 per cent confidence and 95 per cent confidence respectively.

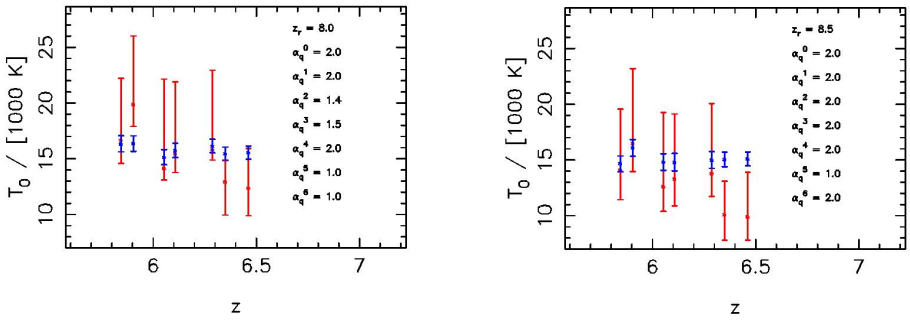

FIGURE 5.3: Model averaged quasar temperature distributions at the maximum a-posteriori estimate of reionisation redshift. We show both the model distributions (blue) and the observed sightlines (red). In both cases, we also include the parameter estimates of $z_{\rm r}$ and $\alpha_{\rm q}^0$ (rightmost point) through $\alpha_{\rm q}^6$ (leftmost point). For clarity, we omit redshift ranges and offset observations 3 and 5 by $z = 0.1$. *Left:* Results obtained for the fiducial near-zone temperature measurements. *Right:* Results for the measurements with addiational Jeans smoothing.

els. Even though this largely ignores the models with the tightest constraints, we may still conclude that $z_{\rm r} > 7.9$ (6.5) to 68 per cent confidence and 95 per cent confidence respectively. This contrasts with recent studies of Lyman Break Galaxies (LBGs, Schenker et al. (2011)) and Lyman Alpha emitters (LAEs Ouchi et al. 2010; Kashikawa et al. 2011), which explain the decline in line emission to high redshift by a corresponding decrease in the ionized hydrogen to $Q \approx 0.5$ by $z = 7$.

These observations could possibly be reconciled with our results by invoking a different source population, such as quasars, to complete reionization or by citing uncertainties in the modelling of temperature. However, we note that all other possible sources of reionization have harder spectra than the Pop II galaxies we consider here and would therefore tend to increase the heating immediately following reionization. Moreover, differences in modelling such as increases in the clumping factor or the power law exponent β would have the same effect. This would then drive IGM temperatures too high to match the Bolton et al. (2011) observations. While it might decrease the asymptotic temperature, since quasar heating would be reduced, this would not change the conclusion that late reionization is unlikely.

Finally we note that, as a sanity check, the optimal temperatures predicted by our model of Population II sources, match quite well to measurements. Figure 5.3 shows the predicted sightline temperature distributions for the maximum aposteriori estimates of $z_{\rm r}$ and $\alpha_{\rm q}^{\rm i}$ compared to the observed quasar temperatures. In the case of the larger Jeans scale measurements, our model predictions do not fit the data well, specifically the high redshift observations, which are systematically low. This is unsurprising as these

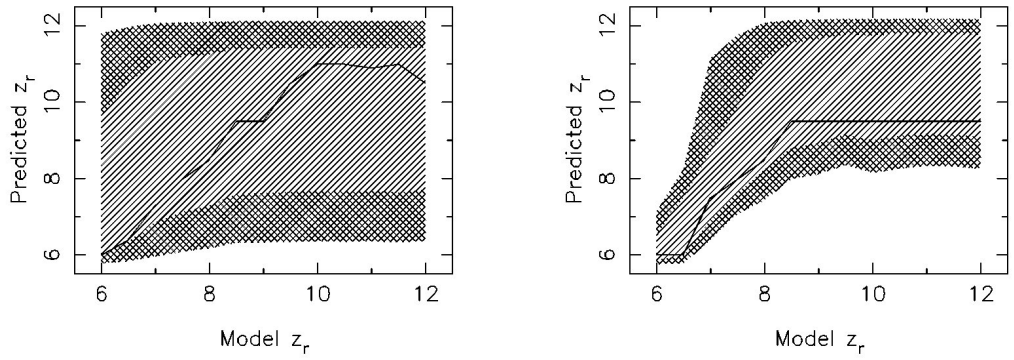

FIGURE 5.4: Bias and uncertainty in the constraints on the reionisation redshift from near-zone temperatures , as a function of the true reionisation redshift in our models. In each case the mode of the predicted posterior distribution is shown (black line) alongside the 68 % (lined region) and 95 % (hatched region) confidence intervals. *Left:* Results assuming 7 temperature measurements *Right:* Results for 100 near-zone temperature measurements, illustrating the optimistic case of large numbers of quasar sight-lines.

measurements are ruled out by a factor of 3. However, for the case of the fiducial model, 4 of the 7 model predictions match well to modes of the observations and 6 fall within the 1-σ limits around the median. There is only truly one outlying point at $z \approx 5.8$, which only rules out our model to approximately 1.5-σ. We do note though that since the temperature measurements decrease by around $5\,000K$ towards high redshift, which is significantly larger than the standard deviation for any model, we can only match the observations this well with a corresponding evolution towards soft quasar spectra. Whether or not this evolution is real, it means that we need to exploit the full range of quasar spectra. Therefore, it seems unlikely that future constraints on the unknown quasar spectral index will be able to significantly tighten our limits on $z_{\rm r}$.

5.2 Constraints from upcoming temperature measurements

In the previous section we presented constraints on the reionization redshift that are available from the existing measurements of temperature. This analysis demonstrates the potential of temperature measurements to constrain reionization, but is currently limited by a lack of statistical significance. However, many more temperature measurements could be made, and inclusion of these will lead to improved constraints. In this section, we investigate how these may improve our constraints.

We begin by creating mock catalogs of possible future observations. To do this, we assume that for a given $z_{\rm r}$, ionising source model, and density bias model, $N_{\rm obs}$ observations are to be drawn. For each one, the quasar spectral index is drawn from the uniform prior over $\alpha_{\rm q}$ and the switch-on time from a uniform distribution in the range $5.8 < z < 6.5$. We note that this effectively excludes the possibility of time evolution in the quasar spectra, however as there is no external evidence of such a rapid evolution, this is a fair assumption. The median of each new observation is taken at random from our predicted temperature distribution for the chosen $z_{\rm r}$, switch-on time and $\alpha_{\rm q}$. Finally, the errors in the measurement around this median are assumed to correspond to one of the 14, 7 fiducial and 7 augmented Jeans scale, observations chosen at random. Once $N_{\rm obs}$ measurements are drawn in this way for each $z_{\rm r}$ and model, we then use equations (5.1) - (5.5) to obtain predicted probability distributions.

This procedure for the generation of mock observations is repeated 100 times, and the resulting distributions are averaged. We then marginalise over the different ionising source models to obtain a predicted distribution $p(z_{\rm r})$ for every $z_{\rm r}$ from which the measurements are drawn. This allows us to estimate the confidence with which the reionization redshift can be measured as a function of the true $z_{\rm r}$. For simplicity, we omit the constraints imposed by $\tau_{\rm CMB}$ in order to assess the new information drawn from the temperature observations alone.

We present our results in Figure 5.4. The left panel show the mode (solid line) and confidence intervals (filled regions) for $N_{\rm obs} = 7$, mimicking the constraints of the previous section. Meanwhile, the right panel shows the same results for a large number of observations[1], $N_{\rm obs} = 100$. We note that, in both cases, the mode typically recovers the true reionisation redshift in the models well, particularly for small $z_{\rm r}$. However, at no reionization redshift do we obtain a particularly tight constraint for seven sight-lines only. For late reionization, this is primarily due to uncertanties in modelling of both the quasar spectrum and the ionizing efficiency. Similarly, if reionization happened early, we will not be able to distinguish well between different $z_{\rm r}$ as the IGM temperature reaches an asymptotic state independent of when reionization occurred. However, increasing the number of observations from 7 to 100 can tighten our constraints on late reionisation considerably, increasing the 95 $\%$ limit from 6.5 to 8.0. This suggests that so long as $z_{\rm r} < 8.0$, temperature measurements and ionising background constraints alone will be able to establish this fact to 95 $\%$ confidence.

On the other hand, pushing the constraints any further than this already very optimistic case is not a realistic possibility. Improved constraints the average quasar EUV spectra index from low redshift data could help to tighten our prior on $\alpha_{\rm q}$, and improve limits at least on late reionisation. However, to tighten constraints on early reionisation

[1]Note that a total of 100 quasar high-resolution spectra at $z \simeq 6$ is a very optimistic scenario. Obtaining one $R \sim 40\,000$ spectrum, even for the brightest known quasars at these redshifts, requires ~ 10 hours of intergration on an 8-m class telescope.

using IGM temperature measurements ultimately requires observations which push to even higher redshifts. The increasing IGM neutral fraction and dwindling number of sufficiently bright quasars at $z > 6$ means this latter case is unlikely. Further progress must therefore be made by using temperature constraints with other measurements, such as the the electron scattering optical depth $\tau_{\rm CMB}$, or constrains on the neutral fraction from the Lyα damping wing and/or Lyα emitters.

Chapter 6

Conclusions

Current understanding of the reionisation history is built on existing observational evidence comprised of measurements of the Gunn-Peterson optical depth at $z \sim 6$, and the electron scattering optical depth of cosmic microwave photons. These measurements respectively probe only the tail end of the epoch of reionisation, and an integral measure of the reionization history. The available constraints therefore permit a wide range of possible histories. Observations of the IGM temperature provide an additional complementary probe since the thermal memory of the IGM yields information at redshifts well beyond the those where observations are made. Measurements of the temperature around high redshift quasars therefore offer a renewed opportunity to constrain the reionisation history of the Universe.

In this paper, we have used the first measurements of IGM temperature at $z > 6$ (Bolton et al. 2010) to constrain the redshift at which the reionisation epoch was ended. Our analysis employs a semi-numerical model for reionisation and heating, which is constrained to fit the CMB electron scattering optical depth, and the ionisation rate inferred from the Lyα forest at $z = 6$. We find that all models which reionise the Universe prior to $z_{\rm r} \approx 9.0$, settle to roughly the same IGM thermal state by $z = 6.0$. The temperature in this asymptotic state is tightly constrained, with a variance of only around $1\,000\mathrm{K}$ at mean density. Moreover, this steady-state temperature is stable to a number of systematic uncertainties in our modelling. In particular, in contrast to the optical depth to electron scattering, it is relatively insensitive to variations in the ionizing photon emissivity as a function of time, which encompasses a range of uncertain parameters including the escape fraction, the stellar IMF and the star formation efficiency.

For scenarios of late reionisation, ($z_{\rm r} < 8.0$), the situation is different since there is significantly more variance in the IGM temperature distribution. This arises partly from differences in ionisation time, which allow for different cooling times and a greater scatter. However, we find that there is always a detectable thermal imprint of at least $2\,500\mathrm{K}$, which differentiates the mean temperature signifying late reionisation from the

asymptotic state achieved for $z_{\rm r} > 9.0$. This implies that measurements of temperature in a quasar proximity zone can be used to constrain the reionisation redshift.

If we assume a constant ionizing photon emissivity, and include the information provided by the CMB electron scattering optical depth, we may conclude that (6.8) $7.4 < z_{\rm r} < 9.0$ (9.8) to 68 $\%$ confidence and 95 $\%$ confidence respectively. When we relax this assumption in our modelling, we significantly weaken these constraints, particularly at the high redshift end, where the IGM temperature provides little information. However, we may still conclude that $z_{\rm r} > 7.9$ (6.5) at the same confidence limits. Furthermore, the inclusion of further measurements in the future should be able to tighten our constraints so that if reionization did happen early, we will be able to rule out $z_{\rm r} < 8.0$ to 95 $\%$ confidence.

In order to push these constraints any further, we would require more certain modelling of the IGM thermal evolution. In particular, the evolution of the ionizing efficiency with redshift would have to be understood in order to narrow the modelling errors on temperature for later reionization scenarios. Additionally, better constraints on the quasar spectral index, if they exist, and a better understanding of the biasing of quasars to high density regions could reduce errors in the modelling of the asymptotic proximity zone temperature. However, even with these reduced modelling uncertainties, temperature measurements will be unable to probe beyond around $z_{\rm r} \approx 9.0$. Alternate observations are necessary to examine the very start of the reionization epoch.

Bibliography

Anninos P., Zhang Y., Abel T., Normal M. L., 1997, New Astronomy, 2, 209

Astier P., Guy J., Regnault N., Pain R., Aubourg E., Balam D., Basa S., Carlberg R. G., Fabbro S., Fouchez D., Hook I. M., Howell D. A., Lafoux H., Neill J. D., Palanque-Delabrouille N., Perrett K., Pritchet C. J., Rich J., Sullivan M., Taillet R., Aldering G., Antilogus P., Arsenijevic V., Balland C., Baumont S., Bronder J., Courtois H., Ellis R. S., Filiol M., Gonçalves A. C., Goobar A., Guide D., Hardin D., Lusset V., Lidman C., McMahon R., Mouchet M., Mourao A., Perlmutter S., Ripoche P., Tao C., & Walton N., 2006, A&A, 447, 31

Bacon D. J., Massey R. J., Refregier A. R., & Ellis R. S., 2003, MNRAS, 344, 673

Barkana R., Loeb A., 2001, Phys. Rep., 349, 125

Becker R. H., Fan X., White R. L., Strauss M. A., Narayanan V. K., Lupton R. H., Gunn J. E., Annis J., Bahcall N. A., Brinkmann J., Connolly A. J., Csabai I., Czarapata P. C., Doi M., Heckman T. M., Hennessy G. S., Ivezić Ž., Knapp G. R., Lamb D. Q., McKay T. A., Munn J. A., Nash T., Nichol R., Pier J. R., Richards G. T., Schneider D. P., Stoughton C., Szalay A. S., Thakar A. R., & York D. G., 2001, AJ, 122, 2850

Becker G. D., Rauch M., Sargent W. L. W., 2007, ApJ, 662, 72

Bolton J. S., Haehnelt M. G., Viel M., Springel V., 2005, MNRAS, 357, 1178

Bolton J. S., Becker G. D., Wyithe J. S. B., Haehnelt M. G., Sargent W. L. W., 2010, MNRAS, 406, 612

Bolton J. S., Haehnelt M. G., 2007, MNRAS, 382, 325

Bolton J. S., Haehnelt M. G., 2007, MNRAS, 374, 493

Bolton, J., Meiksin, A., & White, M. 2004, MNRAS, 348, L43

Bolton, J. S., Oh, S. P., & Furlanetto, S. R. 2009, MNRAS, 395, 736

Bolton J. S., Becker G. D., Raskutti S., Wyithe J. S. B., Haehnelt M. G., Sargent W. L. W., 2011, submitted to MNRAS,

Bond J. R., Cole S., Efstathiou G., Kaiser N., 1991, ApJ, 379, 440

Bond J. R., & Efstathiou G., 1984, ApJ, 285, L45

Boyle B. J., Shanks T., Croom S. M., Smith R. J., Miller L., Loaring N., & Heymans C., 2000, MNRAS, 317, 1014

Bromm V., Kudritzki R. P., Loeb A., 2001, ApJ, 552, 464

Carilli C. L., Wang R., Fan X., Walter F., Kurk J., Riechers D., Wagg J., Hennawi J., Jiang L., Menten K. M., Bertoldi F., Strauss M. A., & Cox P., 2010, ApJ, 714, 834

Choudhury T. R., Ferrara A., 2005, MNRAS, 361, 577

Choudhury T. R., Ferrara A., 2006, MNRAS, 371, L55

Choudhury, T. R., Haehnelt, M. G., & Regan, J. 2009, MNRAS, 394, 960

Ciardi B., Ferrara A., & White, S. D. M., 2003, MNRAS, 344, L7

Coles P., Jones B., 1991, MNRAS, 248, 1

Davis M., Efstathiou G., Frenk C. S., & White S. D. M., 1985, ApJ, 292, 371

Dijkstra M., Haiman Z., Rees M. J., Weinberg D. H., 2004, ApJ, 601, 666

Dunkley J., et al., 2009, ApJS, 180, 306

Efstathiou G., 1992, MNRAS, 256, 43P

Eisenstein D. J., Hu W., 1999, ApJ, 511, 5

Fan X., 2006, ApJ, 132, 117

Faucher-Giguère, C.-A., Lidz, A., Zaldarriaga, M., & Hernquist, L. 2009, ApJ, 703, 1416

Furlanetto S. R., Oh S. P., 2005, MNRAS, 363, 1031

Furlanetto S. R., Oh S. P., 2009, ApJ, 681, 1

Furlanetto S. R., Oh S. P., 2009, ApJ, 701, 94

Geil P. M., Wyithe J. S. B., 2008, MNRAS, 386, 1683

Gnedin N. Y., 2000, ApJ, 535, 530

Gnedin N. Y., & Fan X., 2006, ApJ, 648, 1

Guth A. H., 1981, Phys. Rev. D, 23, 347

Haehnelt M. G., Steinmetz M., 1998, MNRAS, 298, L21

Haiman Z., Loeb A., 1997, ApJ, 483, 21

Hayes M., Schaerer D., Östlin G., Mas-Hesse J. M., Atek H., & Kunth D., 2011, ApJ, 730, 8

Heymans C., Brown M. L., Barden M., Caldwell J. A. R., Jahnke K., Peng C. Y., Rix H.-W., Taylor A., Beckwith S. V. W., Bell E. F., Borch A., Häußler B., Jogee S., McIntosh D. H., Meisenheimer K., Sánchez S. F., Somerville R., Wisotzki L., & Wolf C., 2005, MNRAS, 361, 160

Holtzman J. A., 1989, ApJS, 71, 1

Hui L., Gnedin N. Y., 1997, MNRAS, 292, 27

Hui L., Haiman Z., 2003, ApJ, 596, 9

Iliev I. T., Mellema G., Pen U.-L., Merz H., Shapiro P. R., & Alvarez M. A., 2006, MNRAS, 369, 1625

Kashikawa, N., et al. 2011, ApJ, 734, 119

Komatsu E., Dunkley J., Nolta M. R., et al., 2009, ApJS, 180, 330

Komatsu E., Smith K. M., Dunkley J., et al., 2009, ApJS, 192, 18

Leitherer C. et al., 1999, ApJS, 123, 3

Lidz A., McQuinn M., Zaldarriaga M., Hernquist L., Dutta S., 2007, ApJ, 670, 39

Linde A. D., 1984, Reports on Progress in Physics, 47, 925

Loeb A., 2006, arXiv:astro-ph/0603360

Madau P., Haardt F., & Rees M. J., 1999, ApJ, 514, 648

Madau P., Meiksin A., 1994, ApJ, 433, L53

Mesinger A., 2010, MNRAS, 407, 1328

Mesinger, A. & Furlanetto, S. 2007, ApJ, 669, 663

Miralda-Escudé, J. 2003, ApJ, 597, 66

Miralda-Escude J., Rees M. J., 1994, MNRAS, 266, 343

Miralda-Escudé J., Haehnelt M., & Rees M. J., 2000, ApJ, 530, 1

Mitra S., Choudhury T. R., Ferrara A., 2011, MNRAS, 413, 1569

Ouchi, M., et al. 2010, Accepted in ApJ, arXiv:1007.2961

Pawlik A. H, Schaye J., & van Scherpenzeel E., 2009, MNRAS, 394, 1812

Peebles P. J. E., & Yu J. T., 1970, ApJ, 162, 815

Peebles P. J. E., 1980

Pei Y. C., 1995, ApJ, 438, 623

Perlmutter S., Aldering G., Goldhaber G., Knop R. A., Nugent P., Castro P. G., Deustua S., Fabbro S., Goobar A., Groom D. E., Hook I. M., Kim A. G., Kim M. Y., Lee J. C., Nunes N. J., Pain R., Pennypacker C. R., Quimby R., Lidman C., Ellis R. S., Irwin M., McMahon R. G., Ruiz-Lapuente P., Walton N., Schaefer B., Boyle B. J., Filippenko A. V., Matheson T., Fruchter A. S., Panagia N., Newberg H. J. M., Couch W. J., & The Supernova Cosmology Project, 1999, ApJ, 517, 565

Petitjean P., Webb J. K., Rauch M., Carsell R. F., & Lanzetta K. M., 1993, MNRAS, 262, 499

Press W. HJ., & Schechter P., 1974, ApJ, 187, 425

Pritchard J. R., Loeb A., Wyithe J. S. B., 2009, MNRAS, 408, 57

Quinn T., Katz N., & Efstathiou G., 1996, MNRAS, 278, L49

Raicević M., Theuns T., 2010, accepted to MNRAS

Razoumov A. O., Norman M. L., Abel T., & Scott D., 2002, ApJ, 572, 675

Rees M., 2000

Richards G. T., Croom S. M., Anderson S. F., Bland-Hawthorn J., Boyle B. J., De Propris R., Drinkwater M. J., Fan X., Gunn J. E., Ivezić Ž., Jester S., Loveday J., Meiksin A., Miller L., Myers A., Nichol R. C., Outram P. J., Pimbblet K. A., Roseboom I. G., Ross N., Schneider D. P., Shanks T., Sharp R. G., Stoughton C., Strauss M. A., Szalay A. S., Vanden Berk D. E., & York D. G., 2005, MNRAS, 360, 839

Riess A. G., Strolger L.-G., Tonry J., Casertano S., Ferguson H. C., Mobasher B., Challis P., Filippenko A. V., Jha S., Li W., Chornock R., Kirshner R. P., Leibundgut B., Dickinson M., Livio M., Giavalisco M., Steidel C. C., Benítez T., & Tsvetanov Z., 2004, ApJ, 607, 665

Rubin V. C., Ford W. K. J., & . Thonnard N., 1980, ApJ, 238, 471

Salpeter E. E., 1955, ApJ, 121, 161

Schaye J., Theuns T., Rauch M., Efstathiou G., & Sargent W. L. W., 2000, MNRAS, 318, 817

Schenker, M. A, et al. 2011, Submitted to ApJ, arXiv:1107.1261

Semboloni E., Mellier Y., van Waerbeke L., Hoekstra H., Tereno I., Benabed K., Gwyn S. D. J., Fu L., Hudson M. J., Maoli R., & Parker L. C., 2006, A&A, 452, 51

Sirko E., 2005, ApJ, 634, 728

Sokasian A., Abel T., Hernquist L., & Springel V., 2003, MNRAS, 344, 607

Spergel D. N., Verde L., Peiris H. V., Komatsu E., Nolta M. R., Bennett C. L., Halpern M., Hinshaw G., Jarosik N., Kogut A., Limon M., Meyer S. S., Page L., Tucker G. S., Weiland J. L., Wollack E., & Wright E. L., 2003, ApJS, 148, 175

Spergel D. N., Bean R., Doré O., Nolta M. R., Bennett C. L., Dunkley J., Hinshaw G., Jarosik N., Komatsu E., Page L., Peiris H. V., Verde L., Halpern M., Hill R. S., Kogut A., Limon M., Meyer S. S., Odegard N., Tucker G. S., Weiland J. L., Wollack E., Wright E. L., 2007, ApJS, 170, 377

Springel V., 2005, MNRAS, 364, 1105

Songaila A., Cowie L. L., 2010, ApJ, 721, 1448

Theuns, T., Schaye, J., Zaroubi, S., Kim, T., Tzanavaris, P., & Carswell, B., 2002, ApJ, 567, L103

Thomas, R. M., Zaroubi, S., Ciardi, B., Pawlik, A. H., Labropoulos, P., Jelić, V., Bernardi, G., Brentjens, M. A., de Bruyn, A. G., Harker, G. J. A., Koopmans, L. V. E., Mellema, G., Pandey, V. N., Schaye, J., & Yatawatta, S. 2009, MNRAS, 393, 32

Thoul A. A., & Weinberg D. H., 1996, ApJ, 465, 608

Trac, H., Cen, R., & Loeb, A., 2008, ApJ, 689, L81

Turner M. S., Kolb E. W., 1990

Verner D. A., Ferland G. J., Korista K. T., Yakovlev D. G., 1996, ApJ, 465, 487

Weinberg S., 1972

White R., Becker R., Fan X., Strauss M., 2003, Astron J, 126, 1

Wyithe J. S. B., Bolton J. S., 2010, submitted to MNRAS

Wyithe J. S. B, Hopkins A. M., Kistler M. D., Yuksel H., Beacom J. F., 2010, MNRAS, 401, 2561

Wyithe J. S. B., Loeb A., 2003, ApJ, 586, 693

Wyithe J. S. B., Loeb A., 2007, MNRAS, 375, 1034

Wyithe J. S. B., Morales M. F., 2007, MNRAS, 379, 1647

Zahn, O., Lidz, A., McQuinn, M., Dutta, S., Hernquist, L., Zaldarriaga, M., & Furlanetto, S. R. 2007, ApJ, 654, 12

Zaldarriaga M., Hui L., Tegmark M., 2001, ApJ, 557, 519